minerals

MDPI

Review

Compositional Variations in Apatite and Petrogenetic Significance: Examples from Peraluminous Granites and Related Pegmatites and Hydrothermal Veins from the Central Iberian Zone (Spain and Portugal)

Encarnación Roda-Robles [1,*], Pedro Pablo Gil-Crespo [1], Alfonso Pesquera [1], Alexandre Lima [2,3], Idoia Garate-Olave [1], Enrique Merino-Martínez [4], Joana Cardoso-Fernandes [2,3] and Jon Errandonea-Martin [1]

1 Department of Geology, University of the Basque Country (UPV/EHU), Barrio Sarriena s/n, 48940 Leioa, Spain
2 Department of Geosciences, Environment and Spatial Plannings, Faculty of Sciences, University of Porto, Rua Campo Alegre, 4169-007 Porto, Portugal
3 ICT (Institute of Earth Sciences)—Porto Pole (Portugal), Rua Campo Alegre, 4169-007 Porto, Portugal
4 Department of Geology and Subsurface, Centro Nacional Instituto Geológico y Minero de España (CN IGME—CSIC), C/Ríos Rosas 23, 28003 Madrid, Spain
* Correspondence: encar.roda@ehu.es

check for updates

Citation: Roda-Robles, E.; Gil-Crespo, P.P.; Pesquera, A.; Lima, A.; Garate-Olave, I.; Merino-Martínez, E.; Cardoso-Fernandes, J.; Errandonea-Martin, J. Compositional Variations in Apatite and Petrogenetic Significance: Examples from Peraluminous Granites and Related Pegmatites and Hydrothermal Veins from the Central Iberian Zone (Spain and Portugal). *Minerals* **2022**, *12*, 1401. https://doi.org/10.3390/min12111401

Academic Editor: Nikita V. Chukanov

Received: 28 September 2022
Accepted: 29 October 2022
Published: 1 November 2022

Publisher's Note: MDPI stays neutral with regard to jurisdictional claims in published maps and institutional affiliations.

Abstract: Apatite can be used as an archive of processes occurring during the evolution of granitic magmas and as a pegmatite exploration tool. With this aim, a detailed compositional study of apatite was performed on different Variscan granites, pegmatites and quartz veins from the Central Iberian Zone. Manganese in granitic apatite increases with increasing evolution degree. Such Mn increase would not be related to changes in the fO_2 during evolution but rather to a higher proportion of Mn in residual melts, joined to an increase in SiO_2 content and peraluminosity. In the case of pegmatitic apatite, the fO_2 and the polymerization degree of the melts seem not to have influenced the Mn and Fe contents but the higher availability of these transition elements and/or the lack of minerals competing for them. The subrounded Fe-Mn phosphate nodules, where apatite often occurs in P-rich pegmatites and P-rich quartz dykes, probably crystallized from a P-rich melt exsolved from the pegmatitic melt and where Fe, Mn and Cl would partition. The low Mn and Fe contents in the apatite from the quartz veins may be attributed either to the low availability of these elements in the late hydrothermal fluids derived from the granitic and pegmatitic melts, or to a high fO_2. The Rare Earth Elements, Sr and Y are the main trace elements of the studied apatites. The REE contents of apatite decrease with the evolution of their hosting rocks. The REE patterns show in general strong tetrad effects that are probably not related to the fluids' activity in the system. On the contrary, the fluids likely drive the non-CHARAC behavior of apatite from the most evolved granitic and pegmatitic units. Low fO_2 conditions seem to be related to strong Eu anomalies observed for most of the apatites associated with different granitic units, barren and P-rich pegmatites. The positive Eu anomalies in some apatites from leucogranites and Li-rich pegmatites could reflect their early character, prior to the crystallization of feldspars. The increase in the Sr content in apatite from Li-rich pegmatites and B-P±F-rich leucogranites could be related to problems in accommodating this element in the albite structure, favoring its incorporation into apatite. The triangular plots ΣREE-Sr-Y and U–Th–Pb of apatites, as well as the Eu anomaly versus the $TE_{1,3}$ diagram, seem to be potentially good as petrogenetic indicators, mainly for pegmatites and, to a lesser extent, for granites from the CIZ.

Keywords: apatite; chemical composition; pegmatite; granite; hydrothermal veins; Central Iberian Zone

1. Introduction

The members of the apatite group, with the general formula $Ca_5(PO_4)_3(F,Cl,OH)$, are common accessory phases in a broad range of lithologies, including almost all igneous

rocks. Silicate melts may become apatite-saturated from the earliest [1] until the latest stages of crystallization [2–4], which, combined with the high stability of apatites during the differentiation processes [5–7], allows this phosphate to monitor magmatic evolution [7]. Apatite composition may change to a great extent depending on the physicochemical conditions, as its structure allows for different cationic substitutions. Calcium may be mainly replaced by Mn and Fe and, to a minor extent, by REEs Y, Sr, U, Th and Pb, whereas P may be replaced by Si, S and/or As (e.g., [8], and references therein [7,9–15]). These replacements in the apatite structure depend upon various factors, such as the host rock nature and melt structure, peraluminosity, fO_2 and temperature, among others (e.g., [4,7,8,10,11,15–21]). Therefore, a detailed study of the chemical composition of apatite in igneous environments may give valuable information on the crystallization conditions of its host rocks. Likewise, it may constitute a powerful mineral exploration tool in the case of ore deposits related to igneous rocks (e.g., [10,11,22–26]).

The Central Iberian Zone (CIZ) of the Iberian Massif is characterized by a huge volume of granitic rocks. According mainly to their chemical and mineralogical characteristics, age, protolith and distribution, these granitoids have been classified into five series (e.g., [27,28]). Two of these series (S_1 and S_2), corresponding to highly peraluminous, P-rich, Ca-poor, S-type granites with a metasedimentary source, are commonly associated with significant mineralization of Li, Sn, Nb and/or Ta in pegmatites and/or hydrothermal veins (e.g., [28–34]). Although in some cases it is possible to determine the petrogenetic relationships between granites and these mineralizations, the frequent juxtaposition of different granites in this region shrouds the relationships between them and the above-mentioned mineralizations. Some minerals, including silicates such as micas, alkali feldspars and tourmaline and, less frequently, phosphates (mainly Fe–Mn-bearing ones) have been used as tools to unravel the source for some of these deposit types (e.g., [35–49]). In this study, the compositional variation of apatite from different granitic and pegmatitic lithologies is addressed to evaluate its potential as a petrogenetic indicator in igneous environments and as a pegmatite exploration tool. With this purpose, we compiled a wide chemical dataset (including new analyses and others compiled from the literature) corresponding to: (i) apatite associated with granitic units of different evolution degrees, belonging to the S_1 and S_2 granitic series, considered as parental of the main Li-Sn±Nb±Ta mineralizations from the CIZ; (ii) apatite from barren, P-rich and Li-rich pegmatites; and (iii) apatite from some quartz-rich hydrothermal veins.

2. Geological Setting and Samples

The CIZ is the most internal unit of the Iberian Variscan Belt that constitutes the westernmost part of the European Variscides. It consists of a very thick sequence of Neoproterozoic to lower Cambrian age including, in addition to some orthogneiss units in the northern CIZ domain, shales and sandstones with minor conglomerate, carbonate, and locally some interlayered volcanoclastic rocks (e.g., [50]). Abundant granitoids intruded this sequence [51,52], known as the Schist–Greywacke Complex (see [50], for an overview). The SGC is unconformably overlined by Early Ordovician to Early Carboniferous sediments, which in general are not involved in the Variscan crustal recycling processes.

The granitoids are mainly syn-to post-D_3, which is the last ductile deformation phase recognized in this region and intruded during the period from ≈320 to 295 Ma (e.g., [53–56]). The high degree of thermal maturity attained by the thickened crust, together with the transition from a compressional to a transtensional/transpressional regime, produced an important crustal melting (e.g., [57,58]). Four S-types (S_1, S_2, S_3 and S_4) and one I-type granitic series have been distinguished in the CIZ [27,28]. According to the field, geochemical and geochronological data, only peraluminous granites belonging to the S_1 and S_2 series could be genetically related to the important Li mineralization occurring in pegmatites and in some quartz-rich veins from the CIZ ([28,32]).

Pegmatites of different types, including barren bodies, intermediately evolved pegmatites enriched in P–Be±Nb–Ta, and some highly evolved aplite–pegmatites and granitic

cupolas enriched in Li±Sn±Nb-Ta are relatively common in the CIZ ([28,32] and references therein). These pegmatites occur along a ≈500 km-long by ≈150 km-wide belt with a NNW-SSE strike (Figure 1). They mostly belong to the LCT (Lithium–Cesium–Tantalum) family of the Černý and Ercit classification [59]. Barren and intermediate pegmatites of the CIZ are indistinctly hosted either by the CIZ metasediments or by granitic rocks, whereas most of the highly evolved, Li-rich aplite–pegmatite dykes are hosted by the metasediments (e.g., [28,32,60–66]), with just a few exceptions [67].

Besides pegmatites, Li–Sn–P mineralization in the CIZ may occur associated with quartz-rich hydrothermal veins (Figure 1). These veins usually crosscut the metasediments over leucogranitic cupolas, giving rise to a stockwork structure (e.g., [29,64,68]). Many of these veins were mined for Sn during the last century. Quartz-rich veins enriched in P are much scarcer (e.g., [69,70]).

2.1. S_1 Granites

This suite is mainly constituted by two-mica leucogranites, including the most felsic Variscan granitoids in the CIZ [27,28]. Batholiths belonging to the S_1 suite were mainly emplaced syncinematically (320 ± 6 Ma, on average) and are scarcer afterwards (e.g., [71–74]). This series represents the first important Variscan magmatic event in the CIZ. S_1 granites are mainly restricted to the NCIZ (Figure 1). The P content of these granites may be high, mainly in those outcropping to the south, with mean P_2O_5 values of 0.34 wt.%, whereas their Ca content is generally low (mean contents of 0.77 wt.% CaO, [28]). A pure crustal derivation for these granites has been proposed (e.g., [75,76]), either from peraluminous metaigneous [58,76], metasedimentary [77], or a combination of both sources [73].

For this study, we counted on the chemical data of apatites from the Pereña [47] and Pinilla de Fermoselle S_1 granites, both belonging to the Anatectic Tormes Dome (Figure 1).

2.2. S_2 Granites and Leucogranites

This suite corresponds to P-rich (avg. P_2O_5 = 0.42 wt.%) and Ca-poor (avg. CaO = 0.74 wt.%) highly peraluminous granites [28]. S_2 granitoids present an evident coincidence in isotopic signatures (Sr, Nd, O, Hf) with the hosting metasedimentary sequences of the SGC [78–81]. Their most common facies correspond to biotite ± muscovite ± cordierite ± andalusite/sillimanite monzogranite (≈80%), followed by two-mica ± cordierite ± andalusite/sillimanite leucogranite (≈14%) [27,28]. Most of the batholiths of the S_2 suite are located in the SCIZ (Figure 1) and have been dated with ages in the range ≈310–295 Ma (e.g., [56,78–80,82,83]). These granites are usually emplaced at epizonal levels, under conditions of 2–3 kbar [80,82,84]. S_2 granitoids often form inversely zoned plutons, as is the case of Belvís de Monroy [85,86]. For this study, we analyzed and/or compiled chemical data of apatites from the following S_2 units: (1) Sierra Bermeja [82], Navalmoral de la Mata, Peraleda de San Román, Aldeanueva de Barbarroya, Oropesa, Puente del Arzobispo [86], Logrosán [87] and Guarda-Sabugal [88]; (2) leucogranitic plutons from Belvís de Monroy, Peraleda de San Román, Valdeverdeja and Villar del Pedroso [86]; (3) B-rich leucogranitic units from Belvís de Monroy, Valdeverdeja [86] and Castillejo de Dos Casas; and (4) highly evolved B–P±F-rich leucogranitic units from Belvís de Monroy [86] and Castillejo de Dos Casas.

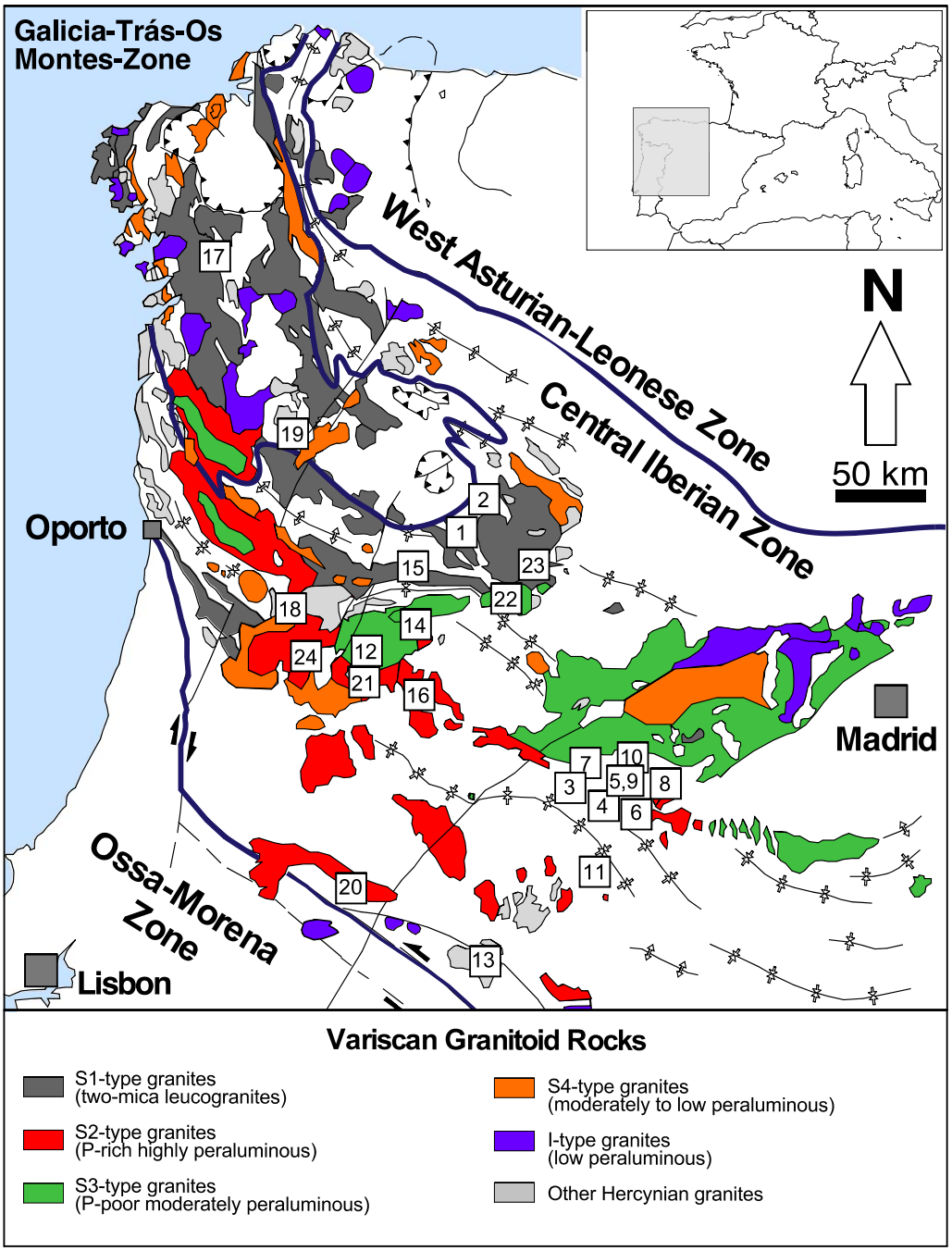

Figure 1. Schematic geological map of the Central Iberian Zone (CIZ) and the Galicia–Trás–Os Montes Zone (GTMZ) (Spain and Portugal) (modified from Martínez-Catalán et al. [89], with the permission of the SGE and authors, and from Roda-Robles et al. [28]) showing the distribution of the five Variscan granitic series proposed in the classification of Villaseca [27] and Roda-Robles et al. [28], and the localities where apatite samples have been taken. Numbers as in Table 1.

2.3. Barren Pegmatites

Barren pegmatites are common in the CIZ. They usually occur as thin tabular bodies with thicknesses <1 m, but more irregular bodies, with thicknesses >15 m are locally observed. The main mineral associations of poorly evolved pegmatites usually contain quartz + alkali feldspars + muscovite ± Fe-tourmaline ± biotite ± garnet ± apatite. They appear either inside granitic plutons, sometimes with gradual contacts between pegmatitic and granitic facies, or hosted by the metasediments of the SGC. In such a case, barren dykes

may be concordant with the schistosity. Often, they exhibit rough internal zoning, with the development of a quartz core. Unidirectional solidification textures, such as tourmaline or mica "combed" crystals and/or quartz + feldspar graphic intergrowths, may be locally observed inside these bodies.

In this study, we selected representative apatite crystals from some barren pegmatites occurring in the Fregeneda–Almendra pegmatitic field (Salamanca, Spain and Guarda, Portugal) [41,65] (Figure 1). These are dyke-like concordant pegmatites hosted by metasediments of the SGC, in the andalusite zone of the contact metamorphism, related to the intrusion of the close Mêda–Escalhão–Penedono–Lumbrales two-mica granite, belonging to the S_1 series. The mineral association consists of quartz, albite, K-feldspar (orthoclase and microcline) and muscovite, with minor Fe–tourmaline, andalusite, chlorite, garnet, biotite, apatite, and accessory Fe–Mn phosphates and oxides of the columbite–tantalite group. These dykes show an internal zonation, with muscovite-rich outer zones and graphic K-feldspar + Fe-tourmaline inner zones. Tourmalinization of the host metasediments in contact with these bodies is a common feature.

Additional chemical data of apatite associated with other barren pegmatites from the region (Figure 1), including Fregeneda–Almendra, Tres Arroyos [90,91], Belvís de Monroy [86], Barroso–Alvão [92] and Navasfrías [33,93], were compiled and included in this study for comparison.

2.4. P-Rich Pegmatites

In the CIZ, the beryl–phosphate-rich pegmatites often occur as isolated bodies, or in groups of just a few pegmatites, in contrast to the pegmatitic fields where Li pegmatites use to occur in groups of dozens to hundreds of bodies (see below). These pegmatites belong to the beryl–phosphate subtype defined in the classification of Černý and Ercit [59]. Some representative samples in the CIZ include Cañada, Pedra da Moura, Senhora da Assunção and Puentemocha pegmatites. Their shape is variable from tabular to turnip-shaped to irregular, with sizes from ≈5 m up to ≈50 m in thickness, and different lengths, usually <100 m. These pegmatites are commonly hosted by anatectic granitic plutons of the S_1 series (Figure 1), often showing a gradual transition between the granitic and the pegmatitic facies. Phosphorous-rich pegmatites show a well-developed internal structure, with a prominent massive quartz core, and coarse-grained size. Major minerals in the beryl–phosphate-rich pegmatites include quartz + K-feldspar + plagioclase + beryl + Fe–Mn phosphates + muscovite ± biotite, whereas schorl, Nb–Ta oxides and apatite are minor or accessory phases. Phosphates are commonly Fe–Mn-rich and usually occur in the intermediate zone as sub-rounded masses up to 1.5 m in diameter.

In this study, apatite samples from the Cañada and Puentemocha beryl–phosphate-rich pegmatites were selected (Figure 1). Both pegmatites are located in the Salamanca province (Spain). The Cañada pegmatite is partly hosted by a S_1 two-mica leucogranitic pluton and partly by a small gabbroic intrusion [94]. The leucogranite is strongly peraluminous, with tourmaline and garnet as common accessory minerals in its most evolved facies. The gabbro predates the granitoids and consists of biotite + hornblende + augite + calcic plagioclase [49,94]. Cañada is a tabular pegmatite with a maximum width of 10 m in outcrop, striking E–W and dipping 60° N [94]. The pegmatite is quite homogeneous in the outcrop. It mainly consists of quartz + plagioclase + K-feldspar + muscovite, with minor tourmaline, biotite, garnet, beryl, and columbite-(Fe). Cassiterite, pyrite, uraninite, corundum, ilmenite, zircon and Fe–Mn carbonates are the main accessory minerals [94]. In the Cañada pegmatite, Fe–Mn phosphates belong to three different associations [49]: (i) the earliest association corresponds to dark masses of up to 30 cm Ø, where phosphates are intergrowth with Fe–Mg silicates (garnet, tourmaline and biotite). Ferrisicklerite is the predominant phosphate in this association, which occurs together with graftonite-(Ca), johnsomervilleite, wagnerite and fluorapatite; (ii) the second phosphate association resembles the first association in color and shape, also with ferrisicklerite as the most common phase. This phosphate often occurs graphically and skeletally intergrown with

graftonite-(Ca). It is also common that ferrisicklerite occurs together with fluorapatite, giving rise to a stripped texture where squared crystals of xenotime-(Y) and monazite-(Ce) appear scattered [46,49]; and (iii) the latest phosphate association occurs as subrounded masses (up to 1 m in diameter) of greyish colors. In this association triphylite containing numerous sarcopside lamellae are the most abundant primary phosphates. No apatite has been identified in this association.

The Puentemocha pegmatite is tabular, with a changing dip from 40° S to subhorizontal, and an estimated size of 7 m thickness by 100 m length [48]. It presents well-developed internal zoning, with a voluminous quartz core, enveloped by an irregular intermediate zone which, in turn, is rimmed by a thinner wall zone that transitions gradually into the hosting granite [48]. The main minerals of Puentemocha pegmatite are quartz + plagioclase + K-feldspar + muscovite + biotite. Beryl is a minor phase, mainly occurring in the outer core and core margin of the pegmatite. Partly replacing the primary zones (mainly intermediate and core zones), some irregular to subrounded greisen masses occur, with muscovite, chlorite and quartz as the main minerals, and with Fe sulphides and struverite as accessory phases. Rounded Fe–Mn phosphate nodules (<8 cm in diameter) are included inside these greisen masses. The main phosphate phases in these nodules include ferrisicklerite, heterosite, sarcopside and alluaudite, with accessory graftonite, eosphorite, rockbridgeite, souzalite and scorzalite. Apatite occurs in pegmatite primary units (intermediate and wall zones) as well as in the hosting granite. It is also common in the phosphate nodules and in the greisen masses [48].

2.5. Li-Rich Pegmatites

This type of pegmatite mainly occurs in the studied region grouped in fields of up to a few hundred bodies [28,32]. Some representative fields from this region are Fregeneda–Almendra, Tres–Arroyos, Barroso–Alvão and Gonçalo ([28,32] and references therein). They are mainly dyke-like bodies, with different dips, from subvertical to subhorizontal, reduced thicknesses (from <50 cm up to ≈30 m), and lengths usually <1 km. Most commonly, these dykes do not present internal zoning. Their grain size is variable, from aplitic to pegmatitic, the biggest crystals being usually <12 cm. Unidirectional solidification textures are frequently observed in these dykes, mainly comb crystals of alkali feldspars and/or Li aluminosilicates, and/or a layering parallel to the contacts with the hosting rock. Quartz + alkali feldspar graphic intergrowths or a quartz core are not commonly observed in these pegmatites. These bodies are usually hosted by metasediments of the SGC and, less frequently, by peraluminous Variscan granites. Only a few pegmatite dykes in each field are Li-rich. In some cases, regional zoning is observed, with the barren pegmatites occurring closer to the associated granite than the Li-richest ones (e.g., Tres Arroyos and Fregeneda–Almendra fields) [32,34,61,95]. In all these dykes albite and quartz are the main minerals, with minor K-feldspar and muscovite, and accessory tourmaline, cassiterite, Nb–Ta oxides, amblygonite–montebrasite group minerals, apatite and Fe–Mn phosphates. Spodumene, petalite and/or Li mica are the main Li ore in the Li-rich bodies, where topaz may also be abundant.

Less commonly, Li mineralization in the CIZ occurs in the apical or marginal areas of highly evolved leucogranites, intruded into the metasediments of the SGC. The most representative Li-bearing cupolas are Pinilla de Fermoselle, Castillejo de Dos Casas and Argemela ([28,32] and references therein). Textures observed in this type of Li mineralization are quite similar to those observed in the Li-rich dykes just described above, including a changing grain size from aplitic to pegmatitic, and the abundance of unidirectional solidification textures such as "combed" crystals and layering. The transition between granitic and pegmatitic facies is commonly gradual [47,96]. The main minerals are quartz, alkali feldspars and micas, with minor tourmaline, topaz, cassiterite, Nb–Ta oxides, Li–Al phosphates, Fe–Mn phosphates and apatite. The main Li ore in the leucogranitic cupolas is lepidolite (for further information on Li-rich pegmatites see [28,32], and references therein).

Apatite samples from some petalite-rich, spodumene + Li–mica-rich and Li–mica-rich dykes from the Fregeneda–Amendra, Queiriga and Navasfrías pegmatitic fields and from the Castillejo de Dos Casas leucogranitic cupola, were analyzed for this study. In addition, chemical data of apatite from Navasfrías [93], Barroso–Alvão [92] and Lalín–Forcarei [97], Li-rich fields and the Pinilla de Fermoselle granitic cupola were compiled for comparison (Figure 1).

2.6. Quartz Veins

In the central area of the CIZ, hydrothermal quartz-rich veins enriched in Sn, Li and P may occur (Figure 1) giving rise to a stockwork over some granitic cupolas belonging to S_1 or S_2 granitic series (e.g., Valdeflórez [68], Golpejas [29], Barquilla [29]) Massueime [98,99] and Feli open pit [64]. These veins are usually thin (<1 m), being hosted in fractures inside the metasediments of the SGC or inside the granites. Together with quartz, minor minerals include alkali feldspars, muscovite, cassiterite and montebrasite, with Nb–Ta oxides, sulphides, apatite and corundum as some common accessory phases. In addition, some barren quartz–rich hydrothermal veins, as well as some quartz-rich, irregular greisenification bodies located inside some pegmatites include apatite crystals.

In this study, representative apatite samples from the Sn-rich Golpejas and Feli quartz veins, as well as from an intragranitic quartz vein from Pinilla de Fermoselle S_1 granite, and greisenification bodies of the Puentemocha pegmatite, were analyzed.

2.7. P-Rich Quartz Veins

Apatite from the P-rich quartz dyke of Sitio do Castelo (Folgosinho, Portugal) was analyzed (Figure 1). This dyke is a tabular sub-vertical body, with a thickness of ≈5 m. It is hosted in Mesquitela granite [69], with a sharp contact between the two lithologies. Three different mineral associations were distinguished in the dyke [100]: (i) Fe–Mn phosphate association, mainly including zwieselite, phosphosiderite and rockbridgeite, with accessory apatite; (ii) quartz + Al mineral association, with muscovite and minor andalusite, garnet tourmaline and gahnite; and (iii) greisen association, with quartz, muscovite, arsenopyrite, scorodite and apatite.

3. Data Collection and Analyses

Overall, in this study close to 750 electron microprobe (major and minor elements) and 260 LA–ICP–MS (trace element) analyses of apatite associated with the different pegmatite, granite and quartz vein types described above were compiled (Table 1). From them, 440 electron microprobe and 120 LA–ICP–MS analyses were taken from the literature. The rest of the electron microprobe data were obtained using a CAMEBAX SX-100 at the Centre de Micro-characterization Raimond Castaing belonging to the Université Paul Sabatier (Toulouse, France). The operating conditions were a voltage of 15 kV and beam current of 20 nA, and the calibration standards used were: SiO_2 (synthetic) (Si), $MnTiO_3$ (synthetic) (Ti, Mn), wollastonite (Ca), corundum (Al), hematite (Fe), albite (Na), orthoclase (K), fluorite (F), graftonite (P), periclase (Mg), chromite (synthetic) (Cr), synthetic glass with Rb_2O = 1.11 wt.% and Cs_2O = 1.89 wt.%, $BaTiO_3$ synthetic (Ba), sphalerite (Zn) and tugtupite (Cl). Data were reduced using the procedure of Pouchou and Pichoir [101], and analytical errors were estimated to be of the order of ±1–2% for major elements and ±10% for minor elements. The structural formulae of apatite were calculated on the basis of 26 (O,F,Cl,OH), H_2O* estimated.

Table 1. Localities and lithologies from which apatite was selected and analyzed for this study. Numbers in the left column correspond to those in the map of Figure 1. References: (1) this work; (2) Merino-Martínez [86]; (3) Pérez-Soba et al. [102]; (4) Vindel et al. [87]; (5) Neiva et al. [88]; (6) Errandonea-Martin [103]; (7) Llorens [93]; (8) Llorens and Moro [33]; (9) Fuertes-Fuente [97]; (10) Martins [92]; (11) Garate-Olave [90].

Locality	S_1 Granites	S_2 Granites	Leucogr.	B-Rich Leucogr.	Highly Fractionated Leucogr.	Barren Pegm.	P-Rich Pegm.	Li-Rich Pegm.	Qz-Veins	P-Rich qz Dyke	Refs.
(1) Puentemocha	X						x		x		(1)
(2) Pinilla de Fermoselle	X						x		x		(1)
(3) Belvís de Monroy			x	x	x	x					(2)(3)
(4) Peraleda de San Román		x	x								(2)
(5) Valdeverdeja			x	x							(2)
(6) Villar del Pedroso		x	x								(2)
(7) Navalmoral de la Mata		x									(2)
(8 Aldeanueva de Barbarroya		x									(2)
(9) Puente del Arzobispo		x									(2)
(10) Oropesa		x									(2)
(11) Logrosán		x							x		(4)
(12) Guarda-Sabugal		x									(5)
(13) Sierra–Bermeja		x									(6)
(14) Castillejo de Dos Casas				x	x			X			(1)
(15) Fregeneda –Almendra						x		X	x		(1)
(16) Navasfrías						x		X			(7)(8)
(17) Lalín–Forcarei								X			(9)
(18) Queiriga								X			(1)
(19) Barroso–Alvão						x		X			(10)
(20) Tres Arroyos						x		X			(11)
(21) Bendada							x				(1)
(22) Cañada							x				(1)
(23) Golpejas									x		(1)
(24) Sitio do Castelo										x	(1)

Our own analyses of trace elements in apatite were conducted by laser ablation inductively coupled plasma mass-spectrometry (LA-ICP-MS) at the Geochronology and Isotope Geochemistry-SGIker facility of the University of the Basque Country UPV/EHU (Spain). During the analyses, minerals mounted on ca. 100 µm thick petrographic sections were ablated with a UP213 Nd:YAG laser ablation system (New Wave) coupled to a Thermo Fisher Scientific XSeries 2 quadrupole ICP-MS instrument, with sensitivity enhanced through a dual pumping system. Spot diameters of ca. 100 µm associated with repetition rates of 10 Hz and laser fluence at the target of ca. 5.5 J/cm^2 were used for analysis. The ablated material was carried in He and then mixed with Ar. The NIST SRM 612 reference glass was used for tuning and mass calibration, by inspecting the signal of 238U to obtain ca. 14,000,000 cps/ppm, and by minimizing the ThO^+/Th^+ ratio to ca. 1%. Raw data were processed using Iolite 2.3 [104,105] and Ca as an internal standard (determined by electron microprobe). Apatite from Cerro Mercado (Durango, Mexico) was used in order to optimize the procedure. This mineral was also used as a secondary standard to control the quality of the results in each analytical session.

4. Results

4.1. Apatite Major Elements

Important differences in major element contents were observed not only among the apatite crystals from the different lithologies, but also in apatite from the same type of rock (Tables 2 and 3). Data of apatite hosted by quartz-rich hydrothermal units (Sn-rich, greisen bodies and intragranitic veins) are very homogeneous, which allows us to include all those data in the same group (quartz veins) for simplification.

Fluorapatite is by far the most common member of the apatites considered in this study, with important variations in the mean F contents depending on lithology (Tables 2 and 3; Figures 2a and 3a–c). The highest mean contents correspond to the apatite from the less evolved granites and the quartz veins (3.74, 3.61; 3.04 wt.% for the S_2 granites, the quartz veins and the S_1 granites, respectively). The lowest F values are found in the Li-rich pegmatites (mean F content of 2.57 wt.%), followed by the highly evolved (B-P±F-rich) leucogranites, with a mean F value of 2.92 wt.%. The Cl concentrations are quite low in general, with mean values < 0.74 wt.%, and the highest contents (4.37 wt.%) corresponding to apatite from the P-rich pegmatites (Figures 2b and 3a–c).

Overall, the widest variations are those observed in apatite from P-rich pegmatites, with CaO values ranging from 37.01 to 55.72 wt.%; P_2O_5 contents between 35.45 and 44.46 wt.%; MnO and FeO contents in the ranges 1.01–10.07 wt.% and 0.23–9.16 wt.%, respectively (Table 3; Figure 2c–f). Apatite from Li-rich pegmatites also shows broad compositional changes, with CaO contents in the range 39.5–55.62 wt.%; P_2O_5 between 34.44 and 43.56 wt.%; MnO and FeO varying from 0.13 to 8.44 wt.% and 0.0 to 9.48 wt.%, respectively. In contrast, apatite associated with granites of the S_1 series shows the narrowest variations (Table 2, Figure 2c–f), with 53.1 to 55.57 wt.% CaO, 42.48 to 43.28 wt.% P_2O_5; 0.07 to 1.33 wt.% MnO; 0.00 to 0.74 wt.% FeO. Apatite associated with quartz veins is also quite homogeneous, with 52.5 to 56.01 wt.% CaO; 37.51–42.91 wt.% P_2O_5; 0–0.85 wt.% MnO and 0.01–0.65 wt.% FeO (Table 3; Figure 2c–f).

The highest mean contents for CaO are observed in apatite from the quartz-rich hydrothermal veins (54.75 wt.%), and from the less evolved granites (54.39, 53.68 and 51.36 wt.% for the S_1 granites, S_2 granites and leucogranites, respectively) (Tables 2 and 3; Figure 2c). Oppositely, the lowest mean CaO values belong to apatite from highly evolved B-P±F-rich leucogranites (47.08 wt.%), followed by P-rich pegmatites (49.00 wt.%) and P-rich quartz veins (49.52 wt.%). The highest mean MnO contents correspond to apatite hosted by P-rich lithologies, with 4.88 wt.% in P-rich pegmatites, and 4.63 wt.% for P-rich quartz veins, with high mean values also for the apatite hosted by highly evolved B-P±F-rich leucogranites (3.99 wt.%) (Tables 2 and 3; Figure 2e). The lowest mean MnO contents are found in apatite associated with the quartz veins (0.43 wt.%), followed by less evolved granitic units (0.52, 0.81 and 1.78 wt.% for the S_2, S_1 and leucogranites, respectively). The highest mean contents of FeO are observed in apatite from highly evolved leucogranites (2.60 wt.%), followed by those from P-rich pegmatites (1.54 wt.%), the lowest values corresponding to apatite from quartz veins (0.24 wt.%), followed by those from less evolved granites (0.48 and 0.55 wt.% for S_1 and S_2, respectively) (Tables 2 and 3; Figure 2f).

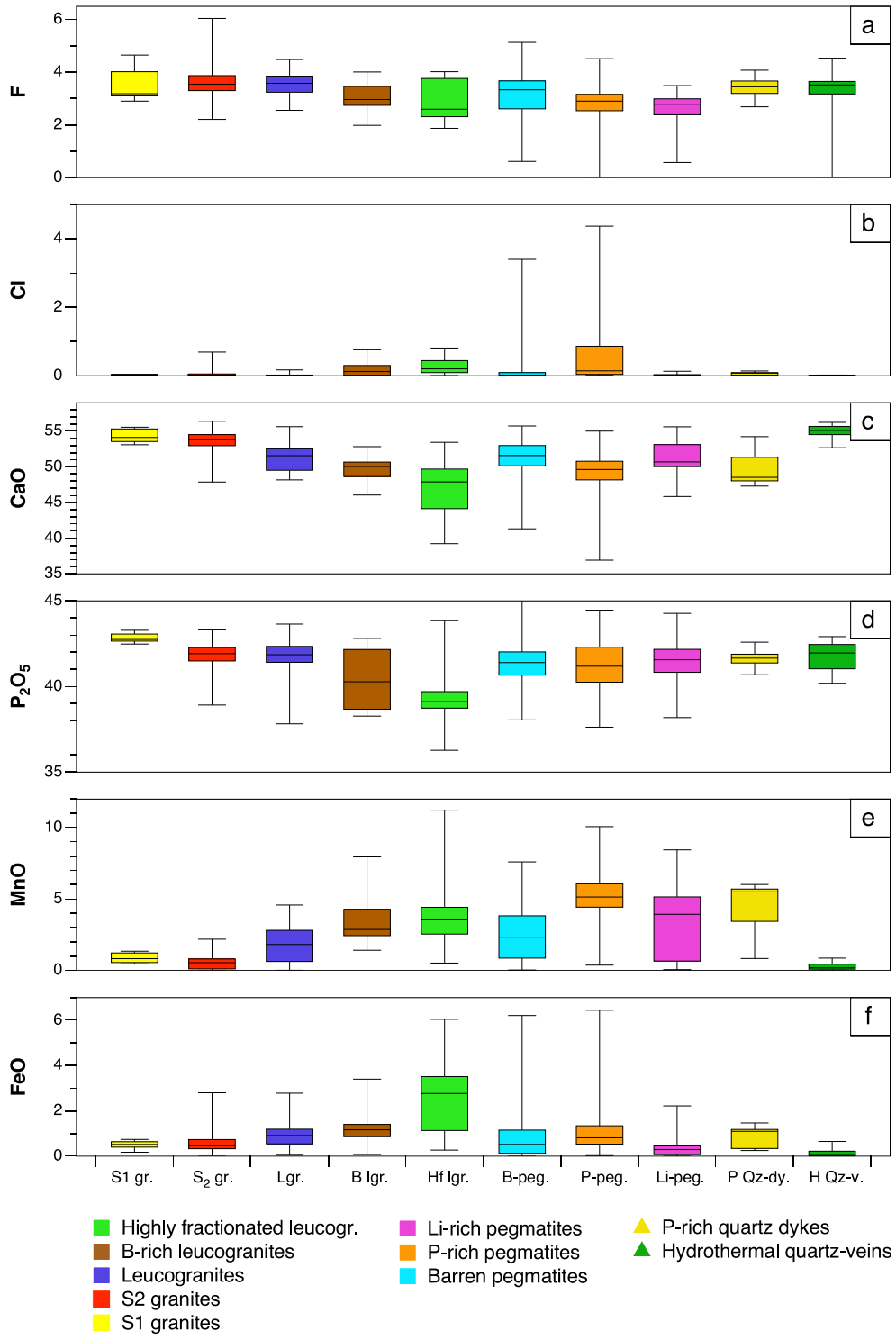

Figure 2. Box and whisker plots for major and minor elements in apatite from the different lithologies. All values in wt.%.

Good negative correlations are observed between Ca and Mn and Ca and Fe (Figure 3d–i). In contrast, P shows no correlation with these elements (Figure 4). In general, Mn values are higher than Fe contents (Figures 3d–l and 4). Na_2O and Al_2O_3 values are low in general (mainly <1 wt.% and <1.5 wt.%, respectively, with few exceptions (Tables 2 and 3). No correlation is found between these elements and other apatite major elements.

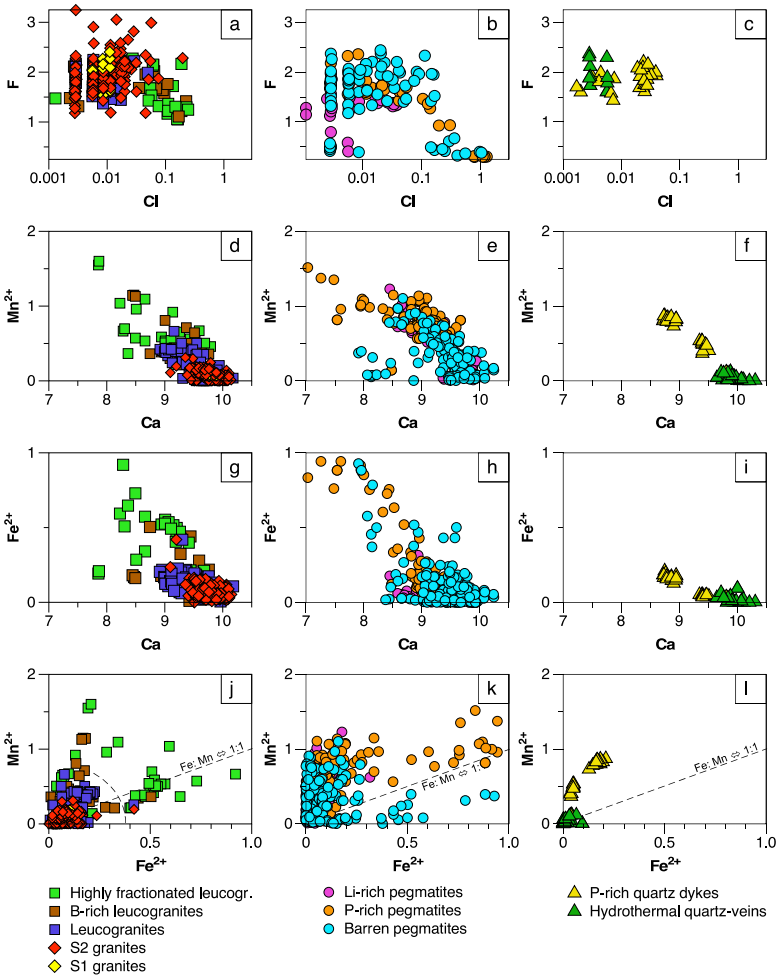

Figure 3. Binary plots of the major and main minor elements for apatite from the different lithologies (all the values in a.p.f.u): (**a**–**c**) Cl versus F; (**d**–**f**) Ca versus Mn; (**g**–**i**) Ca versus Fe; and, (**j**–**l**) Fe versus Mn; in all the cases for granitic, pegmatitic and hydrothermal veins, respectively.

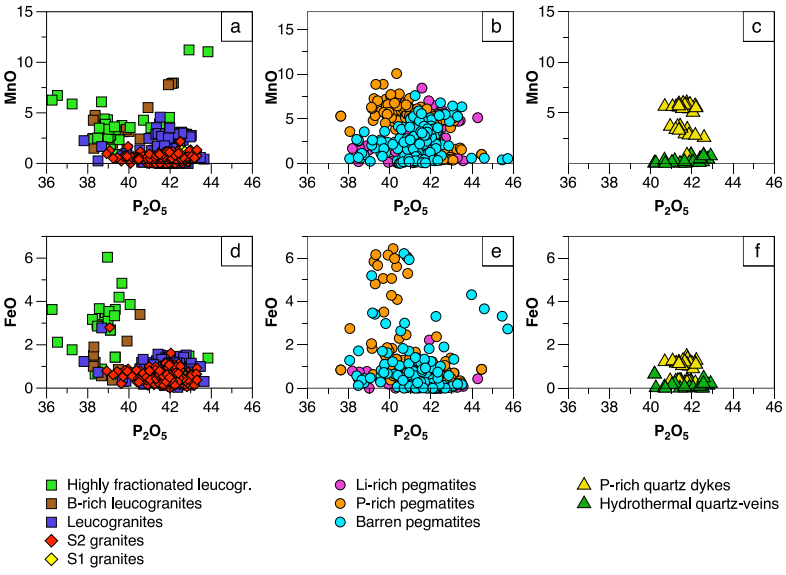

Figure 4. Binary plots of P_2O_5 versus: (**a**–**c**) MnO; and (**d**–**f**) FeO, in apatite from the granitic, pegmatitic and hydrothermal veins, respectively. All the values in wt.%.

Table 2. Representative microprobe analyses with major element composition (wt.%) and unit formula (a.p.f.u.) calculated on the basis of 26 (O,F,Cl,OH), H_2O* estimated, for apatite associated with the different granitic lithologies from the CIZ. Locality number as in Figure 1 and Table 1. References: * this work; ** Merino-Martínez [86]; *** Neiva et al., [88]; **** Errandonea-Martín [103]. b.d.l. below the detection limit.—not analyzed.

Anal. nº	1	2	3	4	5	6	7	8	9	10	11	12	13	14	15
Refs.	*	*	*	**	***	****	**	**	**	*	*	*	*	*	**
Locality	(1)	(1)	(2)	(7)	(12)	(13)	(3)	(5)	(5)	(14)	(14)	(14)	(14)	(14)	(3)
Lithology	S_1 Granites			S_2 Granites			Leucogranites			B-Rich Leucogranites			Highly Fractionates Leucogr.		
SiO_2	b.d.l.	b.d.l.	-	b.d.l.	-	0.03	b.d.l.	b.d.l.	b.d.l.	0.04	0.16	1.02	b.d.l.	b.d.l.	0.22
TiO_2	-	-	-	b.d.l.	0.01	0.02	b.d.l.	b.d.l.	0.02	-	-	0.41	0.16	0.03	0.04
Al_2O_3	b.d.l.	b.d.l.	b.d.l.	0.02	0.09	b.d.l.	b.d.l.	b.d.l.	0.01	b.d.l.	b.d.l.	0.63	0.02	0.01	0.15
FeO(t)	0.74	0.64	0.41	0.49	0.38	0.43	0.75	1.14	0.14	1.19	0.07	1.52	0.31	0.88	3.54
MnO	0.97	1.23	0.51	0.03	0.45	0.77	2.84	1.38	b.d.l.	7.95	2.51	2.46	3.13	6.09	3.38
MgO	b.d.l.	0.04	0.04	b.d.l.	0.02	0.07	b.d.l.	b.d.l.	b.d.l.	b.d.l.	0.01	0.05	b.d.l.	0.02	0.07
ZnO	-	-	-	0.04	-	-	-	0.02	b.d.l.	-	-	0.03	b.d.l.	0.08	b.d.l.
CaO	53.10	53.70	55.57	54.56	53.79	54.28	49.32	51.98	53.66	46.43	51.76	52.83	52.80	47.85	47.29
Na_2O	0.02	b.d.l.	b.d.l.	0.12	0.06	0.05	b.d.l.	0.10	b.d.l.	0.04	b.d.l.	b.d.l.	b.d.l.	0.05	0.74
K_2O	-	-	b.d.l.	b.d.l.	0.06	0.01	b.d.l.	0.01	0.01	-	b.d.l.	0.02	0.01	0.01	0.02
BaO	-	-	-	-	0.03	-	-	-	-	-	-	0.01	b.d.l.	0.09	-
SrO	b.d.l.	b.d.l.	0.04	-	0.02	-	-	-	-	b.d.l.	-	0.20	0.02	0.03	-
P_2O_5	42.65	43.28	43.05	41.41	42.55	41.33	42.34	42.01	42.88	42.16	42.10	38.28	39.73	38.67	39.03
H_2O*	0.27	0.33	0.00	0.07	0.38	0.30	0.00	0.00	0.04	0.41	0.25	0.59	0.00	0.00	0.46
F	3.18	3.10	4.02	3.54	2.95	3.08	3.88	4.00	3.66	2.84	3.13	2.41	3.91	3.84	2.32
Cl	b.d.l.	0.04	0.04	0.04	0.01	0.02	b.d.l.	0.03	b.d.l.	0.00	0.12	0.01	0.21	0.62	0.49
O=F,Cl	1.34	1.31	1.70	1.50	1.24	1.30	1.63	1.69	1.54	1.20	1.35	1.02	1.69	1.75	1.09
Total	99.59	101.05	101.98	98.82	99.56	99.09	97.50	98.98	98.88	99.87	98.76	99.45	98.61	96.52	96.66
Structural formulae on the basis of 26 (O,F,Cl,OH)															
Si	b.d.l.	b.d.l.	-	b.d.l.	-	0.005	b.d.l.	b.d.l.	b.d.l.	0.007	0.027	0.176	b.d.l.	b.d.l.	0.039
Ti	-	-	-	b.d.l.	0.001	0.003	b.d.l.	b.d.l.	0.003	-	-	0.053	0.021	0.004	0.005
Al	b.d.l.	b.d.l.	b.d.l.	0.004	0.018	b.d.l.	b.d.l.	b.d.l.	0.002	b.d.l.	b.d.l.	0.128	0.004	0.002	0.031
Fe^{2+}(t)	0.104	0.089	0.056	0.070	0.053	0.061	0.108	0.162	0.020	0.169	0.010	0.219	0.045	0.131	0.526
Mn^{2+}	0.138	0.173	0.071	0.004	0.064	0.111	0.412	0.198	b.d.l.	1.147	0.361	0.359	0.459	0.919	0.509
Mg	b.d.l.	0.010	0.010	b.d.l.	0.005	0.018	b.d.l.	b.d.l.	b.d.l.	b.d.l.	0.003	0.013	b.d.l.	0.005	0.019
Zn	-	-	-	0.005	-	-		b.d.l.	b.d.l.	-	-	0.004	b.d.l.	0.011	b.d.l.
Ca	9.570	9.540	9.803	9.961	9.688	9.898	9.061	9.452	9.684	8.470	9.426	9.760	9.790	9.137	9.003
Na	0.007	b.d.l.	b.d.l.	0.040	0.020	0.016	b.d.l.	0.033	b.d.l.	0.013	b.d.l.	b.d.l.	b.d.l.	0.017	0.255
K	-	-	b.d.l.	b.d.l.	0.013	0.002	b.d.l.	0.002	0.002	-	b.d.l.	0.004	0.002	0.002	0.005
Ba	-	-	-	-	0.002	-	-	-	-	-	-	0.001	b.d.l.	0.006	-
Sr	b.d.l.	b.d.l.	0.004	-	0.002	-	-	-	-	b.d.l.	-	0.020	0.002	0.003	-
P	6.074	6.076	6.001	5.974	6.056	5.955	6.147	6.036	6.115	6.077	6.058	5.589	5.821	5.835	5.871
F	1.692	1.625	2.093	1.908	1.568	1.658	2.104	2.147	1.950	1.529	1.682	1.314	2.140	2.164	1.304
Cl	b.d.l.	0.011	0.011	0.012	0.003	0.006	b.d.l.	0.009	b.d.l.	0.001	0.035	0.003	0.062	0.187	0.148
OH	0.308	0.363	0.000	0.081	0.429	0.337	0.000	0.000	0.050	0.470	0.282	0.683	0.000	0.000	0.549

Table 3. Representative microprobe analyses with major element composition (wt.%) and unit formula (a.p.f.u.) calculated on the basis of 26 (O,F,Cl,OH), H_2O* estimated, for apatite associated with the different pegmatitic types and hydrothermal quartz veins from the CIZ. Locality number as in Figure 1 and Table 1. b.d.l. below the detection limit.—not analyzed.

Anal. nº	1	2	3	4	5	6	7	8	9	10	11	12	13	14	15
Locality	(15)	(14)	(18)	(21)	(22)	(2)	(15)	(15)	(15)	(1)	(15)	(2)	(24)	(24)	(24)
Lithology	Li-Rich Pegmatites			P-Rich Pegmatites			Barren Pegmatites			Hydrothermal Qz Veins			P-Rich Quartz Dykes		
SiO_2	-	0.07	-	-	-	-	-	-	-	b.d.l.	-	-	0.01	0.01	0.02
TiO_2	-	-	-	b.d.l.	b.d.l.	-	-	-	-	-	-	-	0.02	0.03	0.03
Al_2O_3	-	b.d.l.	b.d.l.	0.05	b.d.l.	b.d.l.	-	-	-	0.02	-	b.d.l.	b.d.l.	0.01	0.00
FeO(t)	0.01	0.29	0.21	0.85	0.83	3.51	0.56	0.21	1.24	0.14	0.06	0.22	0.34	1.20	1.26
MnO	3.98	6.52	5.09	4.70	7.19	5.72	2.66	1.79	4.87	0.41	0.18	0.74	3.65	5.56	5.62
MgO	b.d.l.	b.d.l.	b.d.l.	b.d.l.	b.d.l.	b.d.l.	b.d.l.	b.d.l.	b.d.l.	b.d.l.	b.d.l.	0.02	0.02	<0.01	0.01
ZnO	-	-	-	-	-	-	-	-	-	-	-	-	b.d.l.	0.05	b.d.l.
CaO	50.54	47.93	50.70	49.81	48.03	45.77	52.77	53.36	50.15	55.27	56.25	54.98	51.13	48.02	48.54
Na_2O	0.04	b.d.l.	0.09	0.01	0.11	0.22	0.04	b.d.l.	0.12	b.d.l.	0.02	b.d.l.	0.01	0.03	b.d.l.
K_2O	b.d.l.	-	-	b.d.l.	b.d.l.	b.d.l.	b.d.l.	b.d.l.	b.d.l.	-	b.d.l.	b.d.l.	b.d.l.	0.01	0.01
BaO	-	-	-	-	-	-	-	-	-	-	-	-	0.03	0.03	0.07

Table 3. *Cont.*

Anal. nº	1	2	3	4	5	6	7	8	9	10	11	12	13	14	15
Locality	(15)	(14)	(18)	(21)	(22)	(2)	(15)	(15)	(15)	(1)	(15)	(2)	(24)	(24)	(24)
Lithology	Li-Rich Pegmatites			P-Rich Pegmatites			Barren Pegmatites			Hydrothermal Qz Veins			P-Rich Quartz Dykes		
SrO	0.21	0.19	-	0.02	-	b.d.l.	b.d.l.	0.11	b.d.l.	b.d.l.	b.d.l.	0.07	0.09	b.d.l.	0.28
P_2O_5	42.52	42.09	41.51	41.80	40.42	39.71	41.64	41.80	41.58	42.78	41.64	42.56	41.30	41.37	41.06
H_2O*	0.45	0.54	0.23	0.23	0.46	0.65	0.36	0.63	0.10	0.30	0.00	0.00	0.01	0.00	0.00
F	2.78	2.50	3.22	3.22	2.60	-	2.96	2.41	3.50	3.17	4.40	4.37	3.66	3.73	3.82
Cl	b.d.l.	0.13	-	0.02	0.14	4.10	b.d.l.	b.d.l.	b.d.l.	b.d.l.	b.d.l.	0.02	0.02	0.10	0.06
O=F,Cl	1.17	1.08	1.36	1.36	1.13	0.93	1.25	1.01	1.47	1.33	1.85	1.84	1.54	1.59	1.62
Total	99.36	99.18	99.69	99.35	98.65	98.75	99.74	99.30	100.09	100.76	100.70	101.14	98.74	98.55	99.18
Structural formulae on the basis of 26 (O,F,Cl,OH)															
Si	-	0.012	-	-	-	-	-	-	-	b.d.l.	-	-	0.001	0.001	0.004
Ti	-	-	-	b.d.l.	b.d.l.	-	-	-	-	-	-	-	0.002	0.004	0.004
Al	-	b.d.l.	b.d.l.	0.010	b.d.l.	b.d.l.	-	-	-	0.004	-	b.d.l.	b.d.l.	0.003	0.000
Fe^{2+}(t)	0.001	0.041	0.030	0.121	0.121	0.520	0.079	0.030	0.176	0.019	0.008	0.031	0.049	0.173	0.181
Mn^{2+}	0.571	0.943	0.734	0.679	1.058	0.859	0.382	0.257	0.701	0.058	0.025	0.104	0.530	0.811	0.819
Mg	b.d.l.	b.d.l.	b.d.l.	b.d.l.	b.d.l.	b.d.l.	b.d.l.	b.d.l.	b.d.l.	b.d.l.	b.d.l.	0.005	0.005	0.001	0.003
Zn	-	-	-	-	-	-	-	-	-	-	-	-	b.d.l.	0.006	b.d.l.
Ca	9.166	8.766	9.254	9.098	8.940	8.690	9.587	9.697	9.137	9.852	10.072	9.768	9.398	8.866	8.947
Na	0.013	b.d.l.	0.030	0.003	0.037	0.076	0.013	b.d.l.	0.040	0.000	0.006	b.d.l.	0.005	0.009	b.d.l.
K	b.d.l.	-	-	b.d.l.	b.d.l.	b.d.l.	b.d.l.	b.d.l.	b.d.l.	-	b.d.l.	b.d.l.	b.d.l.	0.003	0.003
Ba	-	-	-	-	-	-	-	-	-	-	-	-	0.002	0.002	0.005
Sr	0.021	0.019	-	0.002	-	b.d.l.	b.d.l.	0.011	b.d.l.	b.d.l.	b.d.l.	0.007	0.009	b.d.l.	0.028
P	6.094	6.083	5.987	6.033	5.945	5.957	5.978	6.002	5.986	6.026	5.891	5.975	5.999	6.036	5.980
F	1.488	1.350	1.735	1.736	1.428	-	1.587	1.293	1.882	1.668	2.325	2.292	1.985	2.033	2.079
Cl	b.d.l.	0.036	-	0.006	0.041	1.231	b.d.l.	b.d.l.	b.d.l.	b.d.l.	b.d.l.	0.006	0.004	0.030	0.019
OH	0.512	0.614	0.265	0.258	0.530	0.769	0.413	0.707	0.118	0.332	0.000	0.000	0.010	0.000	0.000

4.2. Apatite from the P-Rich Puentemocha Pegmatite

As described above, the Puentemocha pegmatite (Salamanca, Spain) is an internally zoned P-rich pegmatite that presents apatite in all its primary (wall and intermediate zones and phosphates nodules) and subsolidus (greisen replacement bodies) units. Moreover, apatite occurs in the host S_1 type granite. This allows a recording of the compositional evolution of apatite during crystallization of this granite–pegmatite system. According to the obtained data, the composition of apatite from the host granite and the wall and intermediate zones of the pegmatite is in the same ranges for its main components, i.e., Ca, Fe, Mn, F and Cl (Table 4, Figure 5). In contrast, apatite from the phosphate nodules is by far the Mn-, Fe- and Cl-richest, and the Ca- and F-poorest, whereas the apatite from the greisenification bodies is the Fe- and Mn-poorest and the Ca-richest (Table 4, Figure 5).

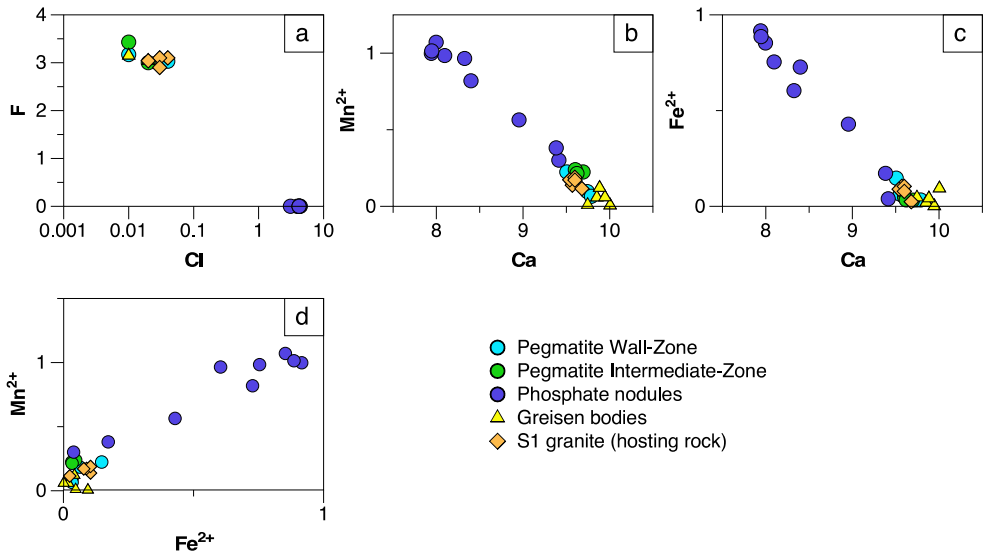

Figure 5. Binary plots for apatite from the different units of the Puentemocha P-rich pegmatite (all the values in a.p.f.u): (**a**) Cl versus F; (**b**) Ca versus Mn; (**c**) Ca versus Fe; and (**d**) Fe versus Mn.

Table 4. Representative microprobe analyses with major element composition (wt.%) and unit formula (a.p.f.u.) calculated on the basis of 26 (O,F,Cl,OH), H_2O* estimated, for apatite associated with the different units distinguished in the Puentemocha pegmatite and in its hosting granite. b.d.l. below detection limit.—not analyzed.

Anal. nº	1	2	3	4	5	6	7	8	9	10	11	12	13	14	15
Lithology		Granite			Wall Zone			Intermediate Zone			Phosphate Nodule			Greissen Masses	
SiO_2	b.d.l.	b.d.l.	b.d.l.	0.02	b.d.l.	b.d.l.	b.d.l.	b.d.l.	b.d.l.	b.d.l.	b.d.l.	b.d.l.	0.01	b.d.l.	b.d.l.
Al_2O_3	b.d.l.	0.02	0.01	b.d.l.	b.d.l.	b.d.l.	b.d.l.	b.d.l.	0.01	b.d.l.	b.d.l.	b.d.l.	0.22	0.02	b.d.l.
FeO(t)	0.64	0.74	0.56	0.45	1.05	0.24	0.23	0.34	0.24	6.14	4.09	5.98	0.65	0.14	0.30
MnO	1.23	1.33	1.21	1.30	1.58	0.46	1.61	1.72	1.54	6.60	6.45	6.76	0.04	0.41	0.85
MgO	0.04	0.01	0.04	0.02	0.05	b.d.l.	b.d.l.	b.d.l.	0.01	0.04	0.00	0.06	b.d.l.	b.d.l.	b.d.l.
CaO	53.70	53.47	53.55	53.45	53.08	54.83	55.02	54.59	54.70	41.53	43.99	41.86	53.80	55.27	54.89
Na_2O	b.d.l.	b.d.l.	0.05	0.06	0.09	0.04	b.d.l.	0.03	0.04	0.34	0.08	0.31	0.34	b.d.l.	0.01
SrO	b.d.l.	0.03	0.03	0.06	b.d.l.	0.04	b.d.l.	0.17	0.10	b.d.l.	b.d.l.	b.d.l.	0.02	b.d.l.	0.26
P_2O_5	43.28	42.58	42.72	42.98	42.67	42.82	43.24	43.42	43.48	39.91	40.36	40.23	40.19	42.78	41.96
H_2O*	0.33	0.34	0.41	0.29	0.35	0.33	0.19	0.31	0.40	0.57	0.64	0.63	0.23	0.30	0.13
F	3.10	3.04	2.90	3.17	3.03	3.09	3.43	3.19	3.00	b.d.l.	b.d.l.	b.d.l.	3.15	3.17	3.48
Cl	0.04	0.02	0.03	0.01	0.04	b.d.l.	0.01	b.d.l.	0.02	4.37	4.18	4.19	0.01	b.d.l.	b.d.l.
O=F,Cl	1.31	1.28	1.23	1.33	1.29	1.30	1.45	1.34	1.27	0.99	0.94	0.95	1.33	1.33	1.47
Total	99.36	99.18	99.69	99.35	98.65	98.75	99.74	99.30	100.09	100.76	100.70	101.14	98.74	98.55	99.18
Structural formulae on the basis of 26 (O,F,Cl,OH)															
Si	b.d.l.	b.d.l.	b.d.l.	0.003	b.d.l.	b.d.l.	b.d.l.	b.d.l.	b.d.l.	b.d.l.	b.d.l.	b.d.l.	0.002	b.d.l.	b.d.l.
Al	b.d.l.	0.004	0.002	b.d.l.	b.d.l.	b.d.l.	b.d.l.	b.d.l.	b.d.l.	b.d.l.	b.d.l.	b.d.l.	0.045	0.004	b.d.l.
Fe^{2+}(t)	0.089	0.104	0.078	0.063	0.147	0.033	0.032	0.047	0.033	0.916	0.604	0.886	0.094	0.019	0.042
Mn^{2+}	0.173	0.189	0.171	0.184	0.224	0.065	0.224	0.239	0.214	0.998	0.965	1.014	0.006	0.058	0.121
Mg	0.010	0.002	0.010	0.005	0.012	0.000	b.d.l.	b.d.l.	0.002	0.011	b.d.l.	0.016	b.d.l.	b.d.l.	b.d.l.
Ca	9.540	9.598	9.599	9.552	9.506	9.789	9.694	9.603	9.622	7.941	8.326	7.946	10.005	9.852	9.884
Na	b.d.l.	b.d.l.	0.016	0.019	0.029	0.013	b.d.l.	0.010	0.013	0.118	0.027	0.106	0.114	b.d.l.	0.003
Sr	b.d.l.	0.003	0.003	0.006	0.000	0.004	b.d.l.	0.016	0.010	b.d.l.	b.d.l.	b.d.l.	0.002	b.d.l.	0.025
P	6.076	6.039	6.051	6.070	6.039	6.041	6.020	6.036	6.044	6.030	6.036	6.034	5.906	6.026	5.970
F	1.625	1.611	1.534	1.672	1.602	1.628	1.784	1.656	1.558	b.d.l.	b.d.l.	b.d.l.	1.729	1.668	1.850
Cl	0.011	0.006	0.009	0.003	0.011	b.d.l.	0.003	b.d.l.	0.006	1.322	1.252	1.258	0.003	b.d.l.	b.d.l.
OH	0.363	0.384	0.457	0.325	0.387	0.372	0.213	0.344	0.437	0.678	0.748	0.742	0.268	0.332	0.150

4.3. Apatite Trace Elements

As with the major elements, some trace element contents in the studied apatite change in a broad range (Table 5). The main variations are observed for Sr, Y and REE (Figure 6a–c). Narrower, but still important, variations are observed for Zr, Li, Zn, Ba, Pb, Ta, Be and U (Figure 6d–k), and slighter variations exist for Hf, Th and Nb (Figure 6l–n). For the rest of the analyzed elements, no remarkable changes are observed. Some of these elements show the same behavior in apatite from pegmatitic and granitic rocks. Such is the case of Sr, REE, Y, U, Zr, Hf, Nb and Ta. Strontium is the only one that shows the highest contents in apatite from the most evolved pegmatites (Li-rich) and leucogranites (Figures 6a and 7). Apatite shows Sr values in the ranges 537–16,400 ppm and 63–527 ppm in Li-rich pegmatites and barren pegmatites, respectively, and changes from 21 to 580 ppm in P-rich pegmatites. The strontium contents in apatite from the most evolved leucogranites are also the highest among granitic rocks (1070–2470 ppm). The lowest values correspond to those of apatite from S_2 granites and leucogranites, where Sr contents change from 10 to 351 ppm and from 1.3 to 991 ppm, respectively (Table 5, Figures 6a and 7a,b). In contrast, apatite from most evolved rocks shows the lowest contents of Y and ΣREE (Table 5, Figure 6b,c and Figure 7). The ΣREE values in apatite are in the ranges 19–1187 ppm, 702–1558 ppm and 536–6291 ppm, for Li-rich, barren and P-rich pegmatites, respectively; and in the ranges <2–3585 ppm, 1979–4396 ppm, 258–5880 ppm and 1350–6275 ppm, for highly evolved leucogranites, B-rich leucogranites, leucogranites and S_2 granites, respectively (Table 5; Figures 6c and 7c,d). The Y contents change in the same way, from <1 to 765 ppm, 332 to 681 ppm and 406 to 9800 ppm for Li-rich, barren and P-rich pegmatites, respectively;

and from <1 to 1930 ppm, 2821 to 2990 ppm, 23 to 3285 ppm and 894 to 3770 ppm, for highly evolved leucogranites, B-rich leucogranites, leucogranites and the S_2 granites, respectively (Table 5; Figures 6b and 7a,b). There is a good positive correlation between Y and ΣREE (Figure 7e,f), whereas Sr exhibits a good negative correlation with Y and ΣREE for granitic apatite and for apatite from pegmatites this negative correlation is not so good (Figure 7a–d).

Table 5. Representative trace element analyses (values in ppm) for apatite associated with the different granitic and pegmatitic lithologies from the CIZ. Locality number as in Figure 1 and Table 1. References: * this work; ** Merino-Martínez [86]; *** Errandonea-Martín [103]; **** Pérez-Soba et al., [102].

Anal. nº	**1**	**2**	**3**	**4**	**5**	**6**	**7**	**8**	**9**	**10**	**11**	**12**	**13**	**14**
Refs.	***	**	****	**	*	*	**	**	*	*	*	*	*	*
Locality	**(13)**	**(7)**	**(3)**	**(3)**	**(14)**	**(14)**	**(3)**	**(3)**	**(15)**	**(15)**	**(22)**	**(22)**	**(15)**	**(14)**
Lithology	**S_2 Granites**		**Leucogranites**		**B-Rich Leucogranites**		**Highly Fractionates Leucogr.**		**Barren Pegmatites**		**P-Rich Pegmatites**		**Li-Rich Pegmatites**	
Li		11.5		11.3	33.0	31.0	65.1	20.7	1.0	1.0	6.6	43.5	2.0	11.0
Be					1.0	0.0	139.0	173.0	1.0	0.0			0.0	1.0
Sc		0.8		1.4	15.0	18.0		16.9	10.0	3.0	4.7	42.4	1.0	0.0
V					0.0	0.0		0.7	1.0		0.7	43.0	0.0	1.0
Cr					2.0	2.0			2.0	1.0	1.1	12.7	1.0	1.0
Co					0.0	0.0		0.1	0.0	0.0	1.0	1.8	0.0	0.0
Ni					2.0	2.0			2.0	2.0	1.5	8.3	2.0	2.0
Cu					1.0				0.0	0.0	0.3	11.9	0.0	0.0
Zn		1.0			8.0	13.0	65.8	135.0	2.0	2.0	68.0	95.0	1.0	1.0
Rb	5.9				1.0	0.0		0.3	0.0	0.0	0.7	38.0	0.0	9.0
Sr	138.5	97.4	73.0	65.6	36.0	32.0	2250.0	1290.0	136.0	733.0	66.9	217.0	7610.0	4366.0
Y	2480.0	2520.0	2900.0	535.0	2817.0	1758.0	9.1	21.8	599.0	456.0	940.0	577.0	24.0	134.0
Zr		0.3		0.3	0.0	9.0	0.7	9.4	5.0	1.0	1.2	184.0	0.0	2.0
Nb	0.6			0.1	0.0	0.0		2.1	0.0	0.0	0.2	4.1	0.0	0.0
Sn					55.0	44.0			3.0	1.0			1.0	3.0
Cs	0.5				0.0				0.0	0.0				2.0
Ba	6.9				2.0	2.0	142.0	199.0	3.0	1.0	34.0	183.0	1.0	7.0
La	247.0	263.0	538.0	253.0	344.0	367.0	1.4	1.2	249.0	201.0	33.0	540.0	26.0	56.0
Ce	1013.0	918.0	1782.0	638.0	793.0	802.0	2.4	7.8	472.0	399.0	230.0	1740.0	42.0	171.0
Pr	153.0	162.0	254.0	80.6	88.0	82.0	0.2	1.4	50.0	38.0	63.9	271.0	4.0	21.0
Nd	770.0	813.0	1073.0	245.0	305.0	258.0	1.0	7.3	158.0	125.0	382.0	1050.0	13.0	87.0
Sm	315.0	320.0	401.0	75.9	152.0	100.0	0.3	3.2	44.0	33.0	319.0	405.0	2.0	19.0
Eu	10.7	7.5	15.2	13.4	3.0	3.0		0.6	5.0	6.0	4.9	6.5	8.0	8.0
Gd	392.0	423.0	480.0	76.2	217.0	116.0	0.8	3.5	46.0	34.0	432.0	289.0	1.0	18.0
Tb	73.7	75.9	102.0	17.0	61.0	32.0	0.1	0.8	11.0	8.0	94.2	48.9	0.0	3.0
Dy	524.0	497.0	636.0	108.0	428.0	228.0	0.8	4.9	76.0	55.0	436.0	211.0	2.0	19.0
Ho	98.0	95.1	97.0	15.3	71.0	40.0	0.2	0.8	14.0	11.0	42.0	19.2	0.0	4.0
Er	242.0	237.0	218.0	35.4	199.0	121.0	0.4	1.7	46.0	36.0	70.0	33.7	1.0	12.0
Tm	30.6	32.9	29.0	5.1	32.0	22.0	0.1	0.2	9.0	7.0	7.3	4.0	0.0	2.0
Yb	175.0	194.0	185.0	35.9	241.0	176.0	0.3	1.4	75.0	57.0	34.9	22.4	3.0	11.0
Lu	20.7	24.4	19.0	4.6	28.0	21.0	0.0	0.1	10.0	8.0	2.8	2.2	0.0	1.0
Hf	0.5		0.2		0.0	0.0		0.3	0.0	0.0	0.4	4.8	0.0	0.0
Ta	0.2	0.0			0.0	0.0	0.0	0.1	0.0	0.0	0.1	0.5	0.0	0.0
Pb		9.0		11.2	16.0	11.0	133.0	4.9	22.0	56.0	103.0	76.7	19.0	11.0
Th		2.9	3.5	8.3	55.0	66.0		0.1	5.0	2.0	1.2	26.5	22.0	13.0
U	72.0	81.4	431.0	258.0	186.0	214.0	1.6	124.0	187.0	229.0	67.0	272.0	3.0	1.0
B							22.3	5.6						
ΣLREE	2498.0	2476.0	4048.0	1292.5	1681.6	1609.1	5.3	20.9	972.2	795.6	1027.9	4006.0	86.9	353.0
ΣHREE	1566.7	1586.8	1781.2	310.9	1280.4	759.1	2.7	13.9	291.7	222.4	1124.1	636.9	17.1	77.6

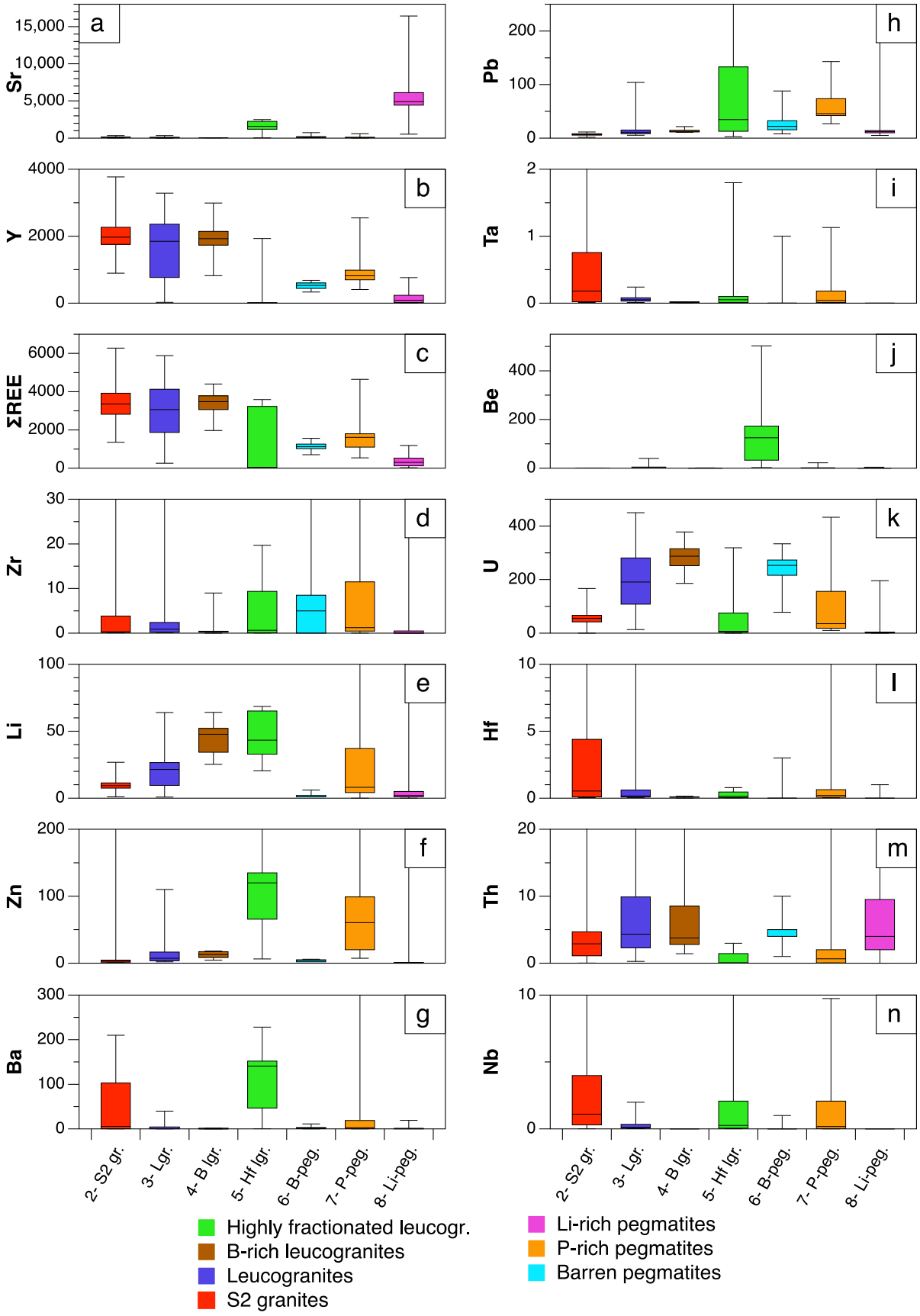

Figure 6. Box and whisker plots for main trace elements in apatite from the different lithologies. All values in ppm.

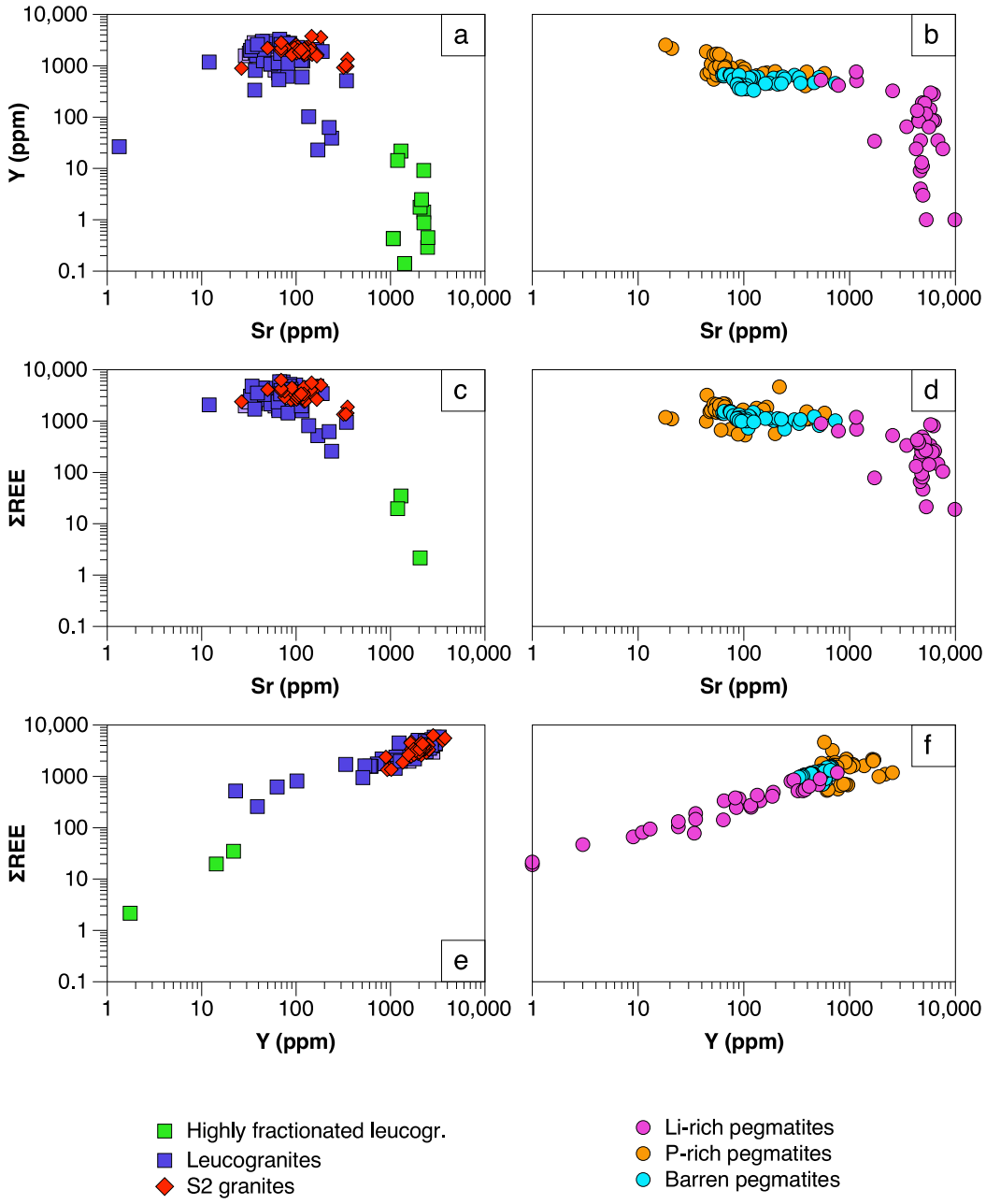

Figure 7. Binary plots of main trace elements in apatite (all values in ppm): (**a**,**b**) Sr versus Y; (**c**,**d**) Sr versus ΣREE; (**e**,**f**) Y versus ΣREE; from the different granitic and pegmatitic lithologies, respectively.

In granitic rocks, the lowest Pb contents correspond in general to apatite from the S_2 granites, whereas some of the highest values are found in the highly evolved leucogranites. Opposingly, the highest U values are found in apatite from the leucogranites and the S_2 granites, and the lowest ones in apatite from the highly evolved leucogranites, which also show the lowest Th contents (Table 5; Figures 6h,k,m and 8a–d). Regarding the pegmatitic apatite, the highest U contents are in apatite from barren pegmatites whereas, in general, the apatite from P-rich pegmatites has the highest Pb and lowest Th contents (Table 5; Figures 6k,h,m and 8a–d). Some pairs of elements, such as Y–Ho, Zr–Hf and Nb–Ta, show in general good positive correlations (Figure 8e–j). However, except for Y–Ho, whose contents decrease with fractionation of the host rocks, an evident relationship between the content variations and the lithology is not found (Table 5; Figures 6d,i,l,n and 8e–j). Lithium, Ba and Be are found in comparable ranges for apatite associated with the different

types of pegmatites, while they seem to increase with fractionation in granitic rocks (Table 5; Figure 6e,g,j).

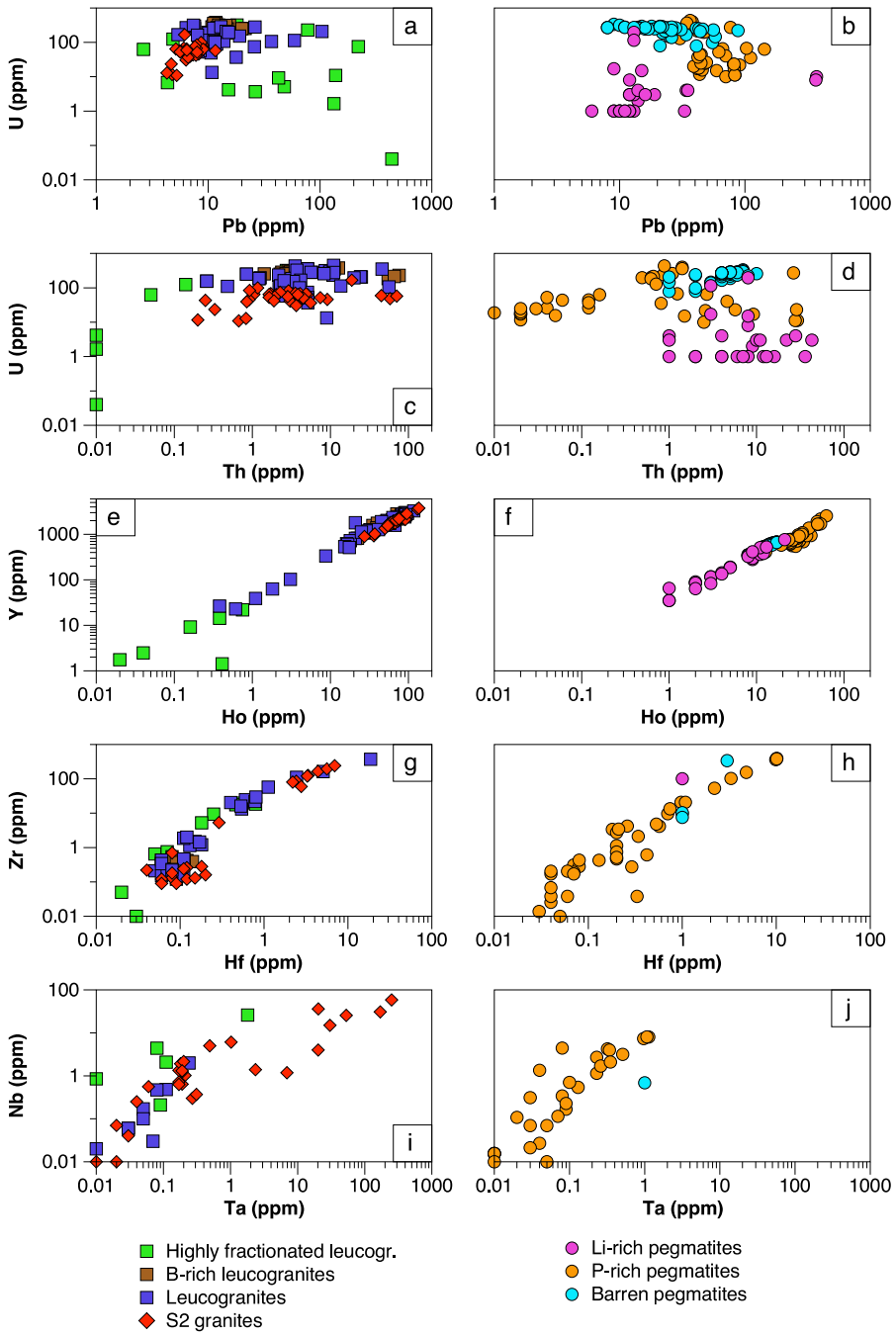

Figure 8. Binary plots of minor trace elements in apatite (all values in ppm): (**a**,**b**) Pb versus U; (**c**,**d**) Th versus U; (**e**,**f**) Ho versus Y; (**g**,**h**) Hf versus Zr; (**I**,**j**) Ta versus Nb; from the different granitic and pegmatitic lithologies, respectively.

4.4. Rare Earth Element Patterns in Apatite

The chondrite-normalized patterns of the studied apatite are notably different for granitic and pegmatitic lithologies. The apatite from the S_2 granites shows quite uniform and well-defined spectra, with a weak slope to the left of the LREE and to the right of the HREE, a strong negative Eu anomaly and no or minor tetrad effects (a split of the chondrite-normalized REE patterns into four segments called tetrads, ref. [16]) (Figures 9a and 10a). Most apatite crystals from the leucogranites show well-defined patterns.

However, mainly in the case of the highly evolved leucogranites, some analyses correspond to erratic patterns of samples that are quite depleted in REE (Figure 9b–d). In general, leucogranitic apatite shows nearly subhorizontal LREE patterns, a negative slope for the HREE, a strong negative Eu anomaly (except for a few apatite crystals that show a positive one), and strong tetrad effects with an M shape (Figures 9b–d and 10a).

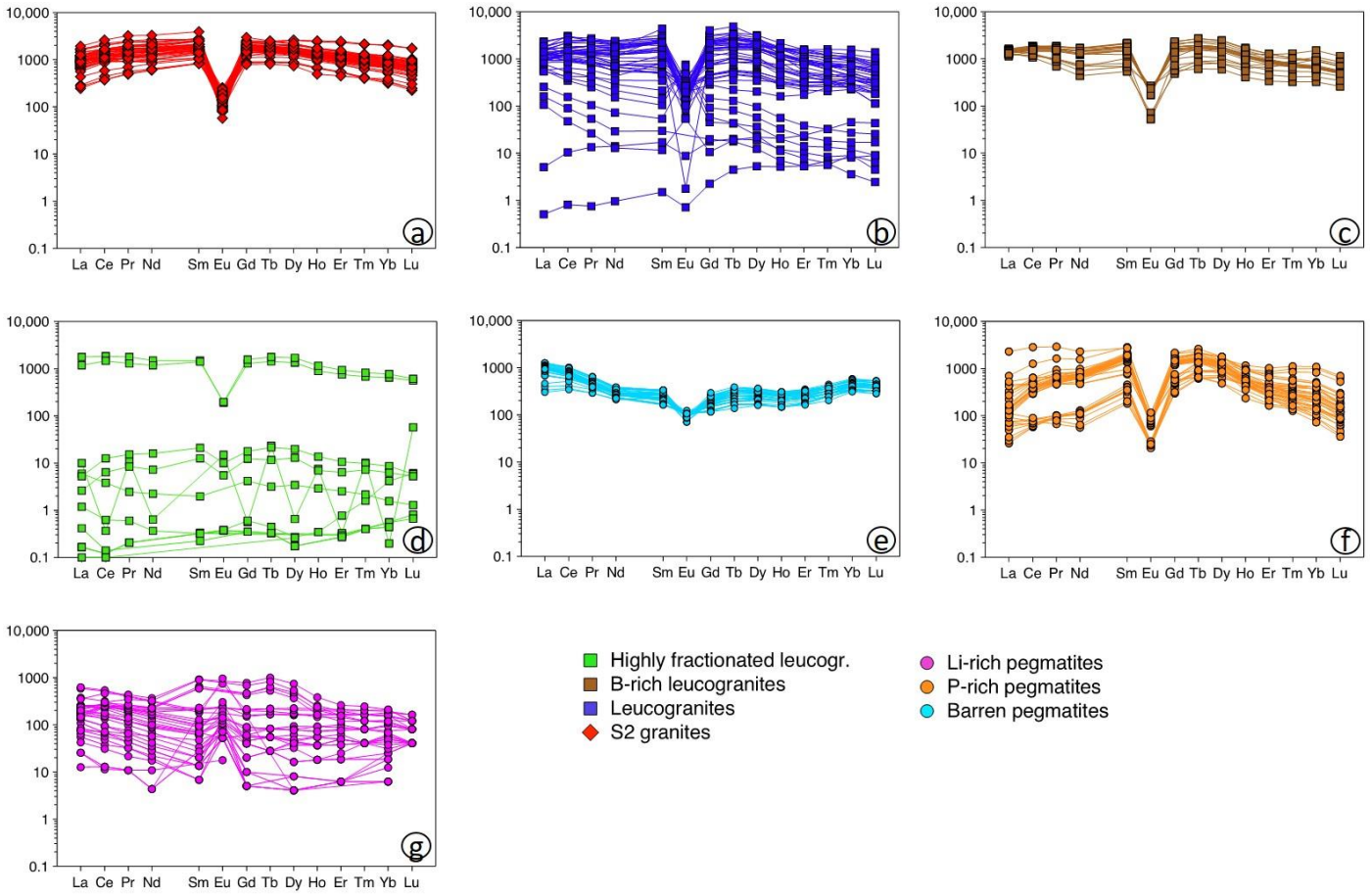

Figure 9. Chondrite-normalized (McDonough and Sun, [106]) apatite REE patterns for: (**a**) S_2 granites, (**b**) leucogranites; (**c**) B-rich leucogranites; (**d**) highly fractionated leucogranites; (**e**) barren pegmatites; (**f**) P-rich pegmatites; and (**g**) Li-rich pegmatites.

The REE spectra for pegmatitic apatite are notably different depending on pegmatite type (Figure 9e–g). In barren and P-rich pegmatites, tetrad effects are strong (Figure 9e,f and Figure 10b). For barren pegmatites, the LREEs show a pronounced negative slope, whereas the HREEs show a weak positive slope, with a not too pronounced negative Eu anomaly (Figure 9e). The apatite from P-rich pegmatites shows a more negative Eu anomaly, with a positive slope for the LREE and a negative slope for the HREE (Figure 9f). The apatite from the Li-rich pegmatites is REE-poorer in general, and often the chondrite-normalized spectra are not well defined. The patterns are quite flat, with no or strongly positive Eu anomaly (Figures 9g and 10b).

Regarding the Ce anomaly, in the granitic apatite from the CIZ the smallest variations correspond to the apatite associated with S_2 granites, and the broadest one to that from the highly evolved leucogranites (Figure 10c). The highest Ce anomalies in the pegmatitic apatite are those observed in P-rich pegmatites, whereas the lowest ones belong to the apatite from Li-rich pegmatites (Figure 10d).

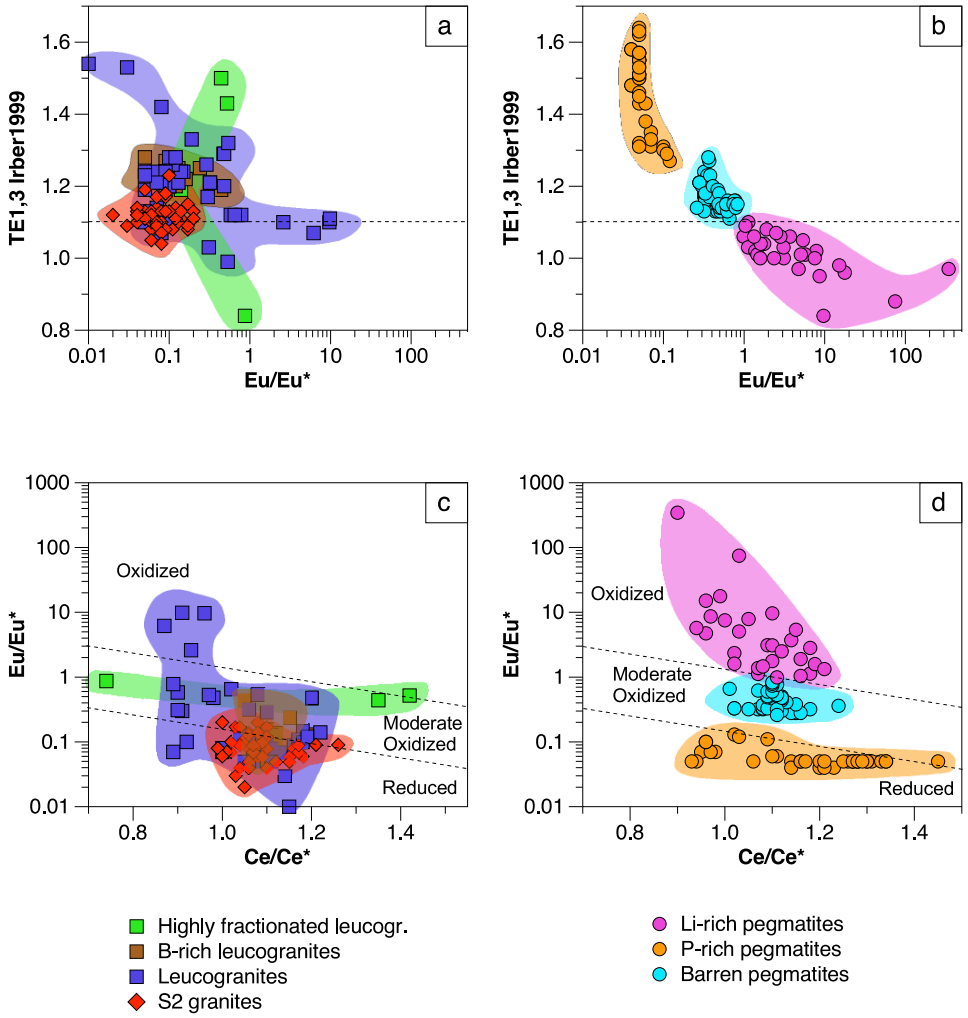

Figure 10. Binary plots of (**a**,**b**) the Eu anomaly (defined as Eu/Eu* = Eun/(Smn × Gdn)0.5) and the Te1,3 value for the tetrad effects calculated according to the procedure of Irber [107]; and (**c**,**d**) the Ce anomaly (defined as Ce/Ce* = Eun/(Lan × Prn)0.5) versus the Eu anomaly; for the apatite from granitic and pegmatitic lithologies, respectively.

5. Discussion

5.1. Significance of Major Element Variations

5.1.1. Manganese and Fe

Apatite can accommodate a number of elements with a wide range of sizes and valence states owing to its structural tolerance and chemical substitution (e.g., [9] and references therein; [10,12,14,15]). Manganese and, to a minor extent, Fe are the main elements that enter into the apatite structure. Their concentration is very variable, from some ppm [10] up to 1.37 Mn a.p.f.u., with Mn substituting preferentially onto Ca1 sites [9]. The highest recorded Mn contents in apatite are ≈19 wt.% MnO [108]. In general, the highest Mn contents are found in apatite from granitic pegmatites and highly evolved peraluminous granites (e.g., [10,91,94,108]). The Mn content in apatite has been proposed to be independent to a great extent of the Mn concentration in the melts [109], whereas fO_2 is considered to have an important influence on Mn incorporation into the apatite structure (e.g., [4,10]). According to these authors, Mn^{2+} may incorporate into apatite more readily than Mn^{3+} or Mn^{4+} because its size and charge are more similar to those of Ca^{2+}. Therefore, in reduced melts the increase in the relative proportion of Mn^{2+} would favor its inclusion into the apatite structure. Nevertheless, the Mn increase in the melts during evolution may obscure the relationships between the fO_2 of the magma and the Mn content

in apatite and, moreover, temperature has a strong influence on the fO_2 of melts [18]. Recent experimental studies indicate that, rather than fO_2, the main factor that controls the apatite melt partition of Mn is the melt structure [20]. A significant increase in the Mn content in apatite has been reported during magmatic evolution for peraluminous granites with high silica contents [7,10,18,109,110]; i.e., Mn would be more easily incorporated into apatite in Si-rich peraluminous melts. This variation in the partitioning of Mn between apatite and melt would be related to the structural changes in the melt. The higher the polymerization of the melt, the lower the availability of free oxygen and the lower the solubility of Mn in the melt, becoming more compatible in the apatite [20,111]. Other factors that could control Mn partition are the pressure, temperature, volatile content in melts, precipitation of mineral phases competing for Mn and melt composition [6,15].

Manganese and Fe contents in apatite associated with granites, pegmatites and quartz veins from the CIZ show significant variations (Tables 2 and 3; Figures 2e,f and 3d,j). The Mn content of granitic apatite noticeably increases with fractionation. S_1 and S_2 granitic series have a main metasedimentary protolith with ilmenite and absent magnetite [28,77–79,81,82,86], which suggests a relatively low fO_2 typical of reducing conditions. Studies on the fO_2 evolution in S-type granitic series from the CIZ [112] indicate reducing conditions close to the Ni-NiO buffer without significant changes during fractionation. This is attested by the presence of some late apatite crystals (not included in this study) in the most evolved leucogranitic unit of the Belvís de Monroy pluton, which are graphite-rich [86,102]. Accordingly, the increase in the Mn content in apatite with the evolution of the granitic melts would not be related to changes in the fO_2 during fractionation. More likely, it would be the result of a higher proportion of Mn in residual melts, joined to an increase in the SiO_2 content and peraluminosity with fractionation, which would change the melt structure reducing Mn solubility and increasing Mn partitioning into apatite.

Apatite associated with pegmatites from the CIZ also shows high Mn and Fe contents (Tables 2 and 3; Figure 2e,f and Figure 3e,h,k). Oppositely to granitic apatite, in general the highest Mn and Fe values are not observed in the most evolved bodies (Li-rich pegmatites), but in the P-rich ones. These P-rich pegmatites belong to the beryl–columbite–phosphate subtype of the LCT family (from Li, Cs and Ta) in the Černý and Ercit classification [59], which corresponds to Si-rich peraluminous pegmatites with intermediate degrees of evolution. In these pegmatites, primary apatite occurs either scattered among silicates in the wall and intermediate zones (as is the case of the Puentemocha pegmatite), or together with other Fe–Mn phosphates within subrounded masses of phosphates. The manganese and Fe contents in apatite change dramatically in both cases, being clearly much higher when apatite grows inside the Fe–Mn phosphate nodules (Figure 5). Redox conditions during pegmatitic crystallization are not completely understood. According to some experimental studies on mica crystallization in leucogranitic and pegmatitic melts [113], biotite would be stable under reducing conditions whereas in oxidizing conditions biotite would be replaced by muscovite, which would be indicative of high fO_2 when occurring as the sole mica. Biotite is present in the host granite of Puentemocha pegmatite and in the wall and intermediate zones [48]. Taking into account that the Mg/(Mg+Fe) value of biotite is sensitive to changes in the oxygen fugacity [114,115], the crystallization of the wall and intermediate zones of the Puentemocha pegmatite has been estimated to take place under relatively reducing conditions at approximately FMQ = −0.5 [48]. Based on the Eu anomaly in apatite from the phosphate nodules (see below), their crystallization also seems to have developed under reducing conditions. Accordingly, Mn and Fe contents in apatite from P-rich pegmatites seem not to be greatly influenced by the redox conditions, as they most probably remained at low fO_2 during the whole pegmatite crystallization. However, there are significant variations in the Mn content between apatite from the wall and intermediate zones and that from the phosphate nodules. Since apatite from P-rich quartz veins (those containing subrounded masses of Fe–Mn phosphates), is also richer in Mn and Fe than the apatite from the other quartz-rich veins (Table 3; Figure 3f,i,l), and both lithotypes are almost free of biotite, it seems plausible that in both cases (P-rich pegmatites and P-rich

quartz dykes) the higher Mn and Fe contents in apatite account for a higher availability of these elements in the system, and not for the redox conditions or the polymerization degree of the fluids. Apart from the silica and alumina contents, the temperature [2,3,116,117] and depth of emplacement [118] may also influence P solubility in silicate melts. Phosphorous behavior in pegmatitic melts has been described as incompatible until the intermediate stages of pegmatitic crystallization (e.g., [47,119–121]), when phosphate saturation occurs, often in the core margin or the outer core zones of the internally zoned pegmatites. The subrounded shape of the phosphate nodules, which are nearly completely constituted by phosphate minerals, has been interpreted as evidence for liquid immiscibility, with those phosphate masses crystallizing from a P-rich melt segregated from a silicate-rich melt (e.g., [47]). A P-enrichment in late-stage magmas may induce liquid immiscibility [122], as previously shown experimentally [123,124]. If immiscibility occurs, then Mn and Fe would most probably partition preferentially into the P-rich melt, as in some pegmatites the only mafic minerals occurring, at least in the inner zones, are the Fe–Mn phosphates. Consequently, and considering that the fO_2 and melt structure seem not to have influenced apatite composition in P-rich pegmatites, we infer that the notoriously higher availability of these transition elements in P-rich melts would lead to higher Mn and Fe contents in apatite from P-rich units. This may also be the case for the apatite from the P-rich quartz dykes.

Most barren pegmatites are aplite–pegmatite bodies or albite-rich leucocratic aplite–pegmatite units in some pegmatitic cupolas at the top of S-type plutons, where the occurrence of mafic minerals is negligible and muscovite is often the only mica. In this scenario, apatite is the main (if not the only) phase competing for Mn and Fe, which could explain the relative abundance of these elements in many apatite crystals associated with barren pegmatites. The same argument may be applied to the apatite from Li-rich highly evolved pegmatites from the CIZ. In these pegmatites the biotite is absent, which together with the positive Eu anomaly of apatite (see below) could indicate oxidizing conditions, typical of hydrous and F-bearing pegmatitic magmas [113]. Therefore, also in this case the fO_2 seems not to have affected to a great extent the Mn (and Fe) content in pegmatitic apatite. Moreover, both barren and Li-rich aplite–pegmatites have in general lower silica values than the S-type granites from the S_1 and S_2 series [28]. This, joined to a higher concentration of fluxes in those pegmatitic melts (mainly H_2O, F and B), would dramatically decrease the polymerization degree of the melts. This means that, as with the fO_2, the melt structure would not have influenced the Mn partition into apatite.

Finally, apatite from the quartz-rich hydrothermal veins shows the lowest Mn and Fe values, except in the case of the P-rich veins already commented on above (Table 3; Figure 3f,i,l). The low Mn and Fe contents in hydrothermal apatite could reflect the low availability of these elements in late hydrothermal fluids exsolved from granitic and pegmatitic melts, as well as the high fO_2, attested by the common coexistence of apatite with oxides, mainly cassiterite, in these veins [113].

5.1.2. F and Cl

Fluorine, Cl and OH may substitute extensively for each other in the halogen site of apatite [9,125,126]. The proportions of these elements depend on different factors including melt (or fluid) composition, occurrence of other F- and Cl-bearing phases such as micas, and P-T conditions ([127]). The fluorine distribution coefficient between fluid and melt is <1 during fractional crystallization [8,128], allowing F to be incorporated into the apatite crystallizing early from the melt [6]. Thus, typical igneous apatite corresponds to fluorapatite [10]. In contrast to F, Cl strongly partitions into the fluid phase when the silicate melt is saturated in H_2O, so chlorapatite becomes the characteristic of the hydrothermal systems [129]. The apatite associated with granites, pegmatites and quartz-rich veins from the CIZ is fluorapatite, except for some apatite crystals occurring inside the phosphate nodules of the P-rich pegmatites (Figure 3b). If these phosphate nodules crystallized as immiscible droplets from an immiscible P-rich melt batch, this could mean that, as with Mn and Fe, Cl would also partition preferentially into such a P-rich melt. None of these

elements were included in the experimental work of Prowatke and Klemme [124], who demonstrated that when silicate melt and phosphate melt immiscibility occurs, Si, Al, Na, K, Ca and large ion lithophile elements partition preferentially into the silicate melt, whereas Sr, LREE, U and Ba tend to be incorporated into the phosphate melt.

5.2. Significance of Trace Element Variations

5.2.1. Eu and Ce Anomalies in Apatite

Besides the major elements Mn and Fe, apatite can accommodate a good number of trace elements via different substitution mechanisms (e.g., [9,10,12,14,15,125]). The REEs, together with Y and Sr, are the main trace elements entering into the apatite structure. Rare Earth Element cations with a trivalent valence state are readily incorporated into this phosphate, whereas Eu (Eu^{2+} and Eu^{3+}) and Ce (Ce^{3+} and Ce^{4+}) may occur with two different oxidation states (e.g., [130,131]). In both cases, the trivalent cations are more compatible with the apatite structure, as the ionic radii of Eu^{3+} and Ce^{3+} are much closer to that of Ca^{2+} [16]. This preference for Eu^{3+} and Ce^{3+} versus Eu^{2+} and Ce^{4+} in the apatite structure may lead to anomalies in the contents of both elements when compared to the other (trivalent) REEs [15], and the Eu and Ce anomalies in apatite may reflect the fO_2 conditions of melts [9,10,15,132]. Accordingly, reducing environments would lead to high Eu^{2+}/Eu^{3+} ratios with pronounced Eu-negative anomalies in apatite, whereas oxidizing conditions would be associated with no or positive Eu anomalies [6,7,9–11,15,109,128,132–134]. A negative Eu anomaly has been postulated to increase with melt evolution ([10]). Nevertheless, the crystallization of other mineral phases, such as feldspars, may strongly influence the Eu distribution, distinguishing the effects of the oxidation state on the Eu anomaly (Eu/Eu*). The high compatibility of Eu^{2+} in feldspar (mainly in K-feldspar, [10]) may control the partitioning of the Eu in the melt [135] and would induce a negative Eu anomaly in apatite if this crystallizes later or grows in the presence of coexisting feldspar ([10,16,109,132,136–138]). Oppositely, Ce anomaly (Ce/Ce*) seems not to be affected by the crystallization of other phases, except for zircon, monazite and other REE-bearing minerals [15]. Low fO_2 would lead to high Ce^{3+}/Ce^{4+} ratios, resulting in a considerable partitioning of Ce^{3+} in apatite and a positive Ce anomaly [6]. Nevertheless, the extent of Ce/Ce* in apatite is usually less pronounced than that of Eu/Eu* [7,10,128,133], and it is assumed to be less effective to measure the redox state of the magma than the Eu anomaly [11]. Some authors propose to combine the variations of two elements with an opposite partitioning behavior into apatite, such as Eu and Ce, in order to assess the redox conditions during apatite crystallization [6,11,134]. In the studied apatite crystals from the granitic and pegmatitic rocks of the CIZ, important variations in the Eu/Eu* (from <0.01 up to 343) are observed, whereas the Ce/Ce* values change in a much narrower range (0.74–1.45) (Figure 10). Apatite associated with granitic rocks shows in general negative Eu anomalies, with the exception of four samples from a leucogranite (Figures 9 and 10). The lowest Eu/Eu* values correspond to apatite from the granite, indicating reducing conditions during its crystallization, although similar REE patterns in apatite from other peraluminous granites have been ascribed to represent the effect of magma mixing, crustal contamination or the influence of a heterogeneous crustal source (e.g., [7]). Apatite from the highly evolved B-P±F-rich leucogranites shows in general less strong Eu anomalies, which could correspond to some higher fO_2 (moderate oxidized in Figure 10c). Apatite from the B-rich leucogranites shows the broadest Eu/Eu* range, falling in the fields of reducing, moderate oxidized and oxidized crystallization conditions in the plot of Figure 10c. This broad range of the Eu anomaly could be indicative of the different crystallization stages of the host rocks under different fO_2. However, as indicated in a previous section of this discussion, the oxidation conditions remain reducing without important changes during fractionation [112]. Therefore, the positive Eu/Eu* anomaly in these apatite crystals could reflect their crystallization prior to that of plagioclase rather than the redox conditions during crystallization, such as suggested by Cao et al. [16] for some apatite crystals from the Koktokay No. 3 pegmatite. Moreover, in these highly fractionated lithologies, K-feldspar

may be very scarce and the plagioclase composition tends to be pure albite, which due to the lack of Ca should include a lower amount of Eu in its structure. Therefore, the early crystallization of apatite, without other important phases competing for Eu, may be the cause of the positive Eu/Eu* values observed in some of the apatite crystals hosted in the leucogranites.

In the case of apatite from pegmatites, their Eu and Ce anomalies allow segregation by pegmatite types (Figure 10). The highest Eu/Eu* and the lowest Ce/Ce* values correspond to apatite associated with P-rich pegmatites, suggesting that apatite formed under reducing conditions. Moreover, the early character of the phosphate masses where these apatite crystals are hosted, in relation to the coexisting plagioclase [49], is not consistent with the Eu negative anomaly in apatite. This means that the origin of the important negative Eu anomaly in apatite from the P-rich pegmatites is likely to be related to the low fO_2 during crystallization. Apatite from the barren pegmatites show intermediate Eu/Eu* and Ce/Ce* values (Figure 10), corresponding to some higher fO_2. Finally, apatite from the Li-rich pegmatites shows strongly positive Eu anomalies and the lowest Ce/Ce* values (Figure 10), which could be attributed to oxidizing conditions. In this case, as with the leucogranites, in the highly evolved pegmatites K-feldspar occurs in low proportions and plagioclase composition corresponds to pure albite, which may host a lower proportion of Eu. Consequently, the early crystallization of apatite could give rise to the positive Eu anomaly observed in most apatite crystals from the Li-rich pegmatites. This implies that fO_2 might not be the only control on the Eu anomaly in this apatite and, hence, redox conditions during Li-rich pegmatite crystallization should not be necessarily highly oxidizing. On the other hand, negative Eu anomalies in extremely fractionated melts, such as that of the Li-rich pegmatites, have been attributed to the high solubility of Eu in comparison with the other REEs in F- and Cl-rich systems [139]. If H_2O saturation is achieved by the melt, then Eu is assumed to be partitioned into the fluid, resulting in a negative Eu anomaly in the apatite crystallizing from the Eu-depleted melt [140,141]. The strong positive Eu anomaly in the apatite of Li-rich pegmatites could reflect that its crystallization occurred at the very early stages of pegmatitic evolution, prior to the early exsolution of fluids. Evidence in support of this is provided by the strong metasomatic effects observed in the host metasediments of these dykes, and by the undercooling-related primary unidirectional textures observed inside most of the Li-rich pegmatites from the CIZ [32].

5.2.2. Strontium and Y Variations

Strontium and Y contents in apatite are considered to be independent of the redox conditions [142], in contrast with Mn, Fe, Eu and Ce. In as much as Sr is compatible with plagioclase, the apatite Sr values have been described as decreasing with magmatic evolution (e.g., [6,7,10,11,15,16,134]). The lowest Sr contents in apatite have been reported in highly evolved granitoids and granitic pegmatites, with values <100 ppm [10]. To the contrary, Y behaves as an incompatible element and, therefore, its content generally increases in apatite with magmatic evolution [6,7,10,11,15], the highest Y contents in apatite (over 1%) being found in granitic pegmatites [10]. Apatite from the granitic and pegmatitic rocks from the CIZ shows important variations for Sr and Y (Figure 7a–f). However, contrary to the just exposed, the Sr-richest apatite is found in the most evolved granitic rocks (highly evolved leucogranites) and in Li-rich pegmatites that, by contrast, show the Y-poorest apatites

The strontium content in apatite seems to reflect the Sr concentration in the whole rock in general with lower Sr values than its host rock rarely exceeding 200 ppm in granitic rocks [7,14,15,129]. As with apatite, the whole-rock data corresponding to Li-rich pegmatites (e.g., [28]) and highly evolved leucogranites from the CIZ (e.g., [86]) also reflect a late Sr increase, being that the Sr values in host leucogranites and pegmatites are lower than in the apatite. Both lithologies are Ca-poor, with pure albite (Ab > 93% mol) being the most common phase together with quartz (e.g., [28,32,86]). Despite Sr being a compatible element in granitic magmas, once these low Ca melts attain high degrees of fractionation,

plagioclase composition becomes Na-rich. Consequently, not being able to enter in plagioclase, the Sr content increases in residual melts. When the crystallization of these highly evolved melts finally occurs, apatite acts as a sink for Sr due to the limitation of albite to incorporate this element. This would also explain that Sr content in apatite is higher than in the whole rock, as no other Sr-bearing minerals coexist there with apatite. According to Watson and Green [143] and Prowatke and Klemme [124], Sr behaves similarly to Eu, which could also explain the positive Eu anomalies found in apatite from the Li-rich pegmatites and in some leucogranitic apatites, where Sr contents are also high. Moreover, the partition coefficients of Sr between apatite and melt are strongly correlated with the CaO content of the melt, with a strong decrease in DSr with increasing CaO [124].

5.2.3. Rare Earth Element Variations

Rare Earth Elements enter into apatite via complex substitutions mainly involving Ca^{2+} and to a lesser extent P^{5+}, Si^{4+} and Na^{+} [9,129,132,144]. The REE patterns of apatite are interpreted to reflect the compositional variation of the host magma [7,15]. However, the REE contents in apatite and in whole-rock are not systematically correlated [129]. According to these authors, the middle REEs incorporate into apatite more easily than the lighter and heavier REEs. In general, as melts become SiO_2-richer, the REE partition coefficients between apatite and melt increase, which could indicate that with evolution, REE contents in apatite increase [16,124]. However, magmatic evolution and the increase in the peraluminosity of the melts would be accompanied by a decrease in the REE content in apatite [15]. Such is the case of the apatite associated with granitic and pegmatitic rocks from the CIZ, which shows a clear REE decrease with evolution (Figures 6c, 7c–f and 9).

In general, most of the studied apatite crystals show marked tetrad effects. In granitic apatite from the CIZ, the tetrad effects become stronger with evolution (Figure 10a), with values of $TE_{1,3} > 1.10$ (calculated according to Irber [107]) for more than half of the apatite crystals associated with the S_2 granites and for most of those occurring in the leucogranites. In the case of pegmatites, the strongest tetrad effects for apatite are found in P-rich pegmatites, followed by the barren pegmatites. In both cases, $TE_{1,3}$ values are >1.10. However, apatite from Li-rich pegmatites shows $TE_{1,3}$ values < 1.2. Some authors have proposed that tetrad effects could be related to a high fluid activity in the melts [107,145–149]. However, in the studied rocks it is more probably a high fluid activity in relation to the most evolved Li-rich pegmatites, which show a stronger metasomatism in the hosting metasediments and effects of subsolidus processes (e.g., tourmalinization of the hosting metasediments [150], albitization of feldspars and greisenization inside pegmatites), than in the S_2 granites. Therefore, in the studied apatite crystals from the CIZ, the extent of tetrad effects seems unrelated to the fluid activity in the system.

Non-CHARAC (CHArge-and- Radius-Controlled) Y/Ho ratios (those out of the range 24–34, [145]) have also been attributed to the abundance of fluids exsolved from melts [16,145,151]. Apatite from S_2 granites and some from less evolved leucogranites show Y/Ho ratios in the CHARAC field (Figure 11a), whereas for pegmatitic apatite, most of that associated with the P-rich pegmatites shows Y/Ho values in this range, while only a few analyses from the Li-rich pegmatites and none from the barren pegmatites fall in that range (Figure 11b). The highest Y/Ho values (up to > 100) correspond to apatite associated with the Li-rich pegmatites, which supports that the non-CHARAC behavior of apatite is characteristic of high-SiO_2 magmatic–pegmatitic systems enriched in H_2O, Li, B, F, P and/or Cl [16,145,152]. Therefore, as suggested by Cao et al. [16], for the Altay Koktokay N°3 pegmatite, the mechanisms controlling the tetrad effects and the non-CHARAC Y/Ho behavior in apatite are different, the former most probably being independent of the fluid activity.

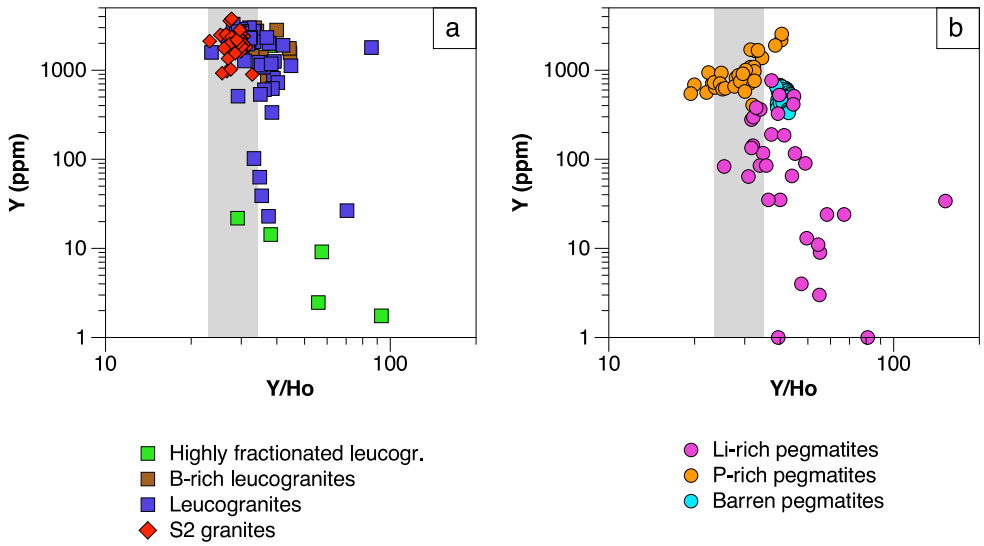

Figure 11. Binary plot of Y/Ho versus Y in apatite from (**a**) granitic; and (**b**) pegmatitic lithologies. The greyish area represents the region where Y/Ho ratios correspond to CHARAC values.

5.3. Apatite as Archive of Processes in Granitic and Pegmatitic Systems

A good number of studies have concluded that apatite is a key mineral in magmatic–hydrothermal systems to record their crystallization history and to reflect the melt composition and oxidation conditions [2,4,6–8,10,11,15,17,21,124,132,153]. Moreover, compositional variations of apatite may help to determine the economic potential and fertility index in different ore deposit environments, including granitoids (e.g., [7,10,134]); pegmatites, (e.g., [10,16,49,154,155]); carbonatites (e.g., [10,23]); skarns (e.g., [11]); Sn, W and Mo deposits (e.g., [6,11]); Cu-porphyry [156,157]; and Au-epithermal deposits [26] among others.

For this purpose, a detailed compositional study of apatite associated with different granitic and pegmatitic rocks from the CIZ was performed to assess the potential of apatite as a recorder of the processes involved in the formation of granitic and pegmatitic rocks. Iron and Mn in the apatite of different granites seem to reflect the evolution degree of their host rocks (Figure 3j), with the highest values being associated with the highest degrees of evolution. The apatite of pegmatitic rocks mostly has Mn content higher than Fe content. Only the apatite from some barren pegmatites is richer in Fe than in Mn (Figure 3k). Therefore, a higher Fe than Mn content in apatite could indicate a low degree of evolution in the host pegmatite. However, the opposite (higher Mn than Fe values) does not necessarily mean that the pegmatite is more evolved. Clearly, apatite from the phosphate nodules of the P-rich pegmatites shows the highest Fe+Mn contents, in some cases > 1.5 apfu. The apatite from the quartz veins is in general very Fe- and Mn-poor, which allows discriminating it from the apatite from the P-rich quartz veins, which shows Fe+Mn values > 0.30 a.p.f.u. (Figure 3l).

In the Sr, Y and REE diagram, apatite from Li-rich pegmatites and evolved leucogranites plot close to the Sr corner, whereas the rest of the apatite crystals are in general closer to the REE vertex (Figure 12a,b). Only a few samples from the P-rich pegmatites are richer in Y than in Sr and REE. Slighter differences are found among U, Th and Pb (Figure 12c,d). In pegmatites, apatite from Li-rich bodies is undoubtedly the poorest in U, showing in general higher Pb than Th contents. Apatite from P-rich pegmatites is Th-poor, usually with higher Pb than U contents. Apatite from the barren pegmatites is the U-richest and the Th- and Pb-poorest. Apatite from granitic units is noticeably richer in U than in Pb and Th. Only a few samples associated with leucogranitic rocks show higher contents of Pb than of U.

In the Eu anomaly versus $TE_{1,3}$ plot (Figure 10b), apatites from the three pegmatite categories are clearly discriminated, with that from the Li-rich pegmatites showing the strongest Eu (positive) anomalies and less marked tetrad effects as calculated by Irber [107], whereas the opposite values correspond to apatite from the P-rich pegmatites, and intermediate values to the barren pegmatites. For granitic apatite this plot is not so discriminant,

but still apatite from the leucogranites shows either the highest $TE_{1,3}$ values or the highest Eu anomaly (Figure 10a).

All these plots are potentially interesting for using apatite as a petrogenetic indicator, at least for S_2 granites and leucogranites and for the pegmatites from the CIZ. Nevertheless, further investigation is necessary to specify and contrast its usefulness in other granitic–pegmatitic belts worldwide.

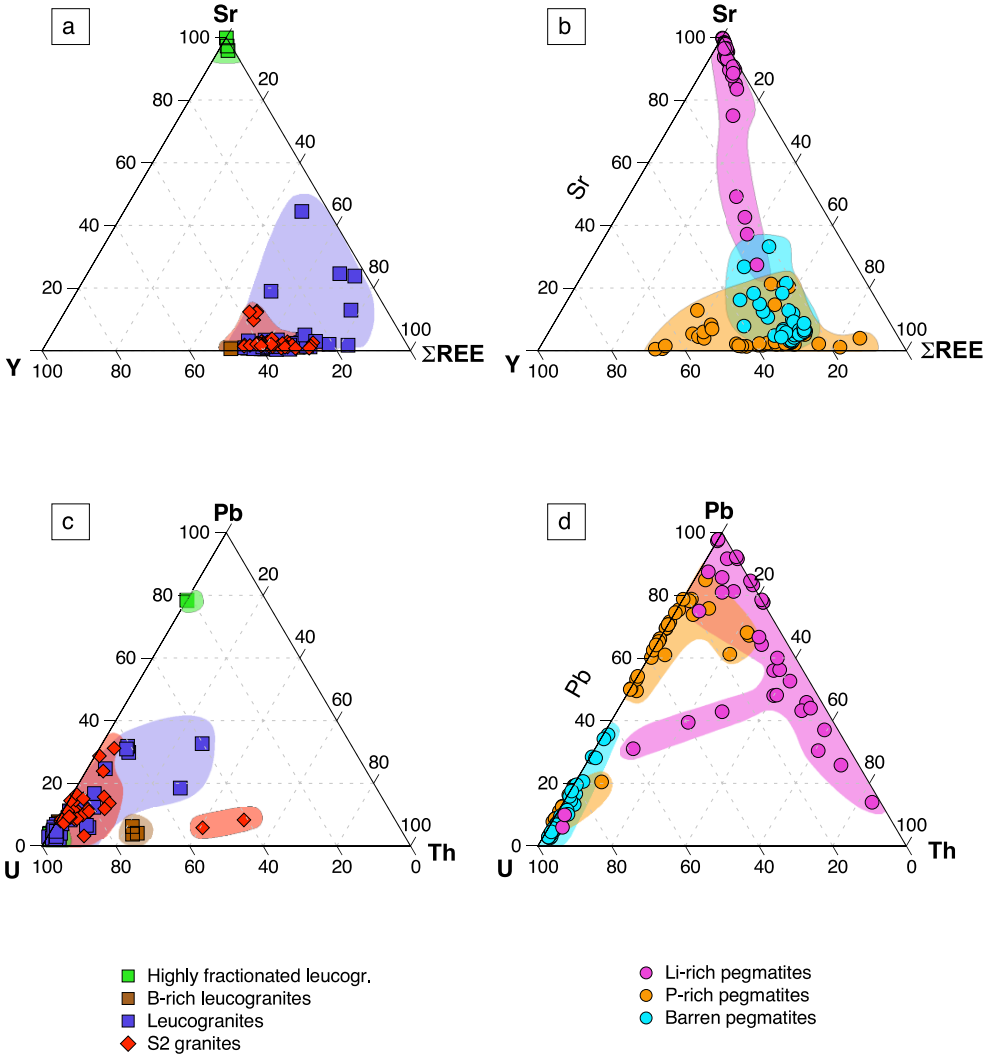

Figure 12. Triangular plots for apatite: (**a**,**b**) Sr-Y-ΣREE; and (**c**,**d**) Pb-U-Th, for the granitic and pegmatitic lithologies, respectively.

6. Summary and Conclusions

(1) Apatite is a minor to accessory ubiquitous mineral in granitic and pegmatitic rocks. Here we present a systematic study on the composition of apatites associated with different Variscan granites, pegmatites and quartz veins from the CIZ.

(2) Except for the minor occurrence of chlorapatite in P-rich pegmatites, most of the studied apatites correspond to fluorapatite. Important chemical variations have been found in apatite depending on the host lithology and evolution degree. Mn and Fe are the major elements whereas REE, Sr and Y are the main trace components in the apatite structure. While the highest Mn and Fe contents are found in the apatite from P-rich pegmatites, followed by the apatite from the P-rich quartz veins, the lowest values correspond to quartz veins and peraluminous granites. This may be attributed

either to the low availability of Mn and Fe in late fluids exsolved from granitic and pegmatitic melts or to a high fO_2.

(3) Pegmatitic apatite with Fe/Mn > 1 may be indicative of the barren nature of its hosting pegmatite.
(4) The Mn and Fe in granitic apatite increase with increasing evolution degree, probably due to a higher concentration of Mn in residual melts, together with an increase in SiO_2 content and peraluminosity, rather than changes in fO_2.
(5) In the case of pegmatitic apatite, the fO_2 and the polymerization degree of the melts seem not to have influenced the Mn and Fe content, but the higher availability of these transition elements and/or the lack of minerals competing for them.
(6) The apatite from the P-rich pegmatites often appears together with Fe–Mn phosphates occurring in subrounded nodules, which probably crystallized from a P-rich fluid exsolved from the pegmatitic melt. If immiscibility took place, Mn, Fe and Cl would partition preferentially into the P-rich melt.
(7) The apatite from the quartz-rich hydrothermal veins is the Mn- and Fe-poorest one, which may be attributed either to the low availability of these elements in late hydrothermal fluids exsolved from granitic and pegmatitic melts, or to a high fO_2.
(8) The REE contents in apatite decrease with the evolution degree of their hosting rocks, whereas the highest Sr and lowest Y contents are found in the most evolved lithologies (Li-rich pegmatites and B-P±F-rich leucogranites).
(9) The REE patterns generally show strong tetrad effects, which do not seem to depend on the activity of fluids in the system. These, on the contrary, likely drive the non-CHARAC behavior of apatite from the most fractionated granites and pegmatites.
(10) The strong Eu anomalies observed for most apatites associated with different granites, barren and P-rich pegmatites are interpreted to be related to low fO_2 conditions. The positive Eu anomalies of some apatites from leucogranites and Li-rich pegmatites could reflect their early character, prior to the crystallization of feldspars.
(11) The increase in Sr in apatite from most Li-rich pegmatites and B-P±F-rich leucogranites is the result of the limitation of albite for hosting appreciable amounts of Sr in its structure, thus being incorporated into apatite
(12) The triangular ΣREE-Sr-Y and U-Th-Pb plots, as well as the Eu anomaly versus $TE_{1,3}$ diagram, are potentially good discriminant tools, mainly for pegmatites from the CIZ.

Author Contributions: Conceptualization and investigation, E.R.-R., A.P. and P.P.G.-C.; Writing—original draft preparation, E.R.-R.; Writing—review and editing, E.R.-R., A.P., P.P.G.-C., A.L., I.G.-O., E.M.-M., J.C.-F. and J.E.-M.; Visualization, E.R.-R.; Project administration, E.R.-R.; Funding acquisition, E.R.-R. All authors took part in the fieldwork. All authors have read and agreed to the published version of the manuscript.

Funding: Financial support was provided by the European Commission's Horizon 2020 Innovation Programme (grant agreement No 869274, project GREENPEG: New Exploration Tools for European Pegmatite Green-Tech Resources); by Ministerio de Ciencia e Innovación and Agencia Estatal de Investigación (Project RTI2018-094097-B-100, with ERDF funds, A way of making Europe); and by the University of the Basque Country UPV/EHU (grant GIU18/084). The work was also supported by Portuguese National Funds through the FCT–Fundação para a Ciência e a Tecnologia, I.P., with projects UIDB/04683/2020 and UIDP/04683/2020-ICT (Institute of Earth Sciences).

Data Availability Statement: Data are available in Tables 2–5.

Acknowledgments: The authors are very grateful to the editor Axel Müller for the invitation to write this article. The constructive reviews of two anonymous reviewers are very much appreciated.

Conflicts of Interest: The authors declare no conflict of interest.

References

1. Hoskin, P.W.O.; Kinny, P.D.; Wyborn, D.; Chappell, B.W. Identifying accessory mineral saturation during differentiation in granitoid magmas: An integrated approach. *J. Petrol.* **2000**, *41*, 1365–1396. [CrossRef]

2. Bea, F.; Fershtater, G.B.; Corretgé, L.G. The geochemistry of phosphorus in granite rocks and the effect of aluminium. *Lithos* **1992**, *29*, 43–56. [CrossRef]
3. Pichavant, M.; Montel, J.M.; Richard, L.R. Apatite solubility in peraluminous liquids: Experimental data and an extension of the Harrison-Watson model. *Geochim. Cosmochim. Acta* **1992**, *56*, 3855–3861. [CrossRef]
4. Miles, A.J.; Graham, C.M.; Hawkesworth, C.J.; Gillespie, M.R.; Hinton, R.W. Evidence for distinct stages of magma history recorded by the compositions of accessory apatite and zircon. *Contrib. Mineral. Petrol.* **2013**, *166*, 1–19. [CrossRef]
5. Lisowiec, K.; Slaby, E.; Götze, J. Cathodoluminescence (CL) of apatite as an insight into magma mixing in the granitoid pluton of Karkonosze, Poland. In Proceedings of the Conference on Raman and Luminescence Spectroscopy in the Earth Sciences, Wien, Austria, 3–6 July 2013.
6. Azadbakht, Z.; Lentz, D.; McFarlane, C. Apatite Chemical Compositions from Acadian-Related Granitoids of New Brunswick, Canada: Implications for Petrogenesis and Metallogenesis. *Minerals* **2018**, *8*, 598. [CrossRef]
7. Chu, M.-F.; Wang, K.-L.; Griffin, W.L.; Chung, S.-L.; O'Reilly, S.Y.; Pearson, N.J.; Iizuka, Y. Apatite Composition: Tracing Petrogenetic Processes in Transhimalayan Granitoids. *J. Petrol.* **2009**, *50*, 1829–1855. [CrossRef]
8. Piccoli, P.; Candela, P. Apatite in Igneous Systems. *Rev. Mineral. Geochem.* **2002**, *48*, 255–292. [CrossRef]
9. Pan, Y.; Fleet, M.E. Compositions of the Apatite-Group Minerals: Substitution Mechanisms and Controlling Factors. *Rev. Mineral. Geochem.* **2002**, *48*, 13–49. [CrossRef]
10. Belousova, E.A.; Griffin, W.L.; O'Reilly, S.Y.; Fisher, N.I. Apatite as an indicator mineral for mineral exploration: Trace-element compositions and their relationship to host rock type. *J. Geochem. Explor.* **2002**, *76*, 45–69. [CrossRef]
11. Cao, M.; Li, G.; Qin, K.; Seitmuratova, E.Y.; Liu, Y. Major and trace element characteristics of apatites in granitoids from central Kazakhstan: Implications for petrogenesis and mineralization. *Resour. Geol.* **2012**, *62*, 63–83. [CrossRef]
12. Teiber, H.; Marks, M.A.W.; Arzamastsev, A.A.; Wenzel, T.; Markl, G. Compositional variation in apatite from various host rocks: Clues with regards to source composition and crystallization conditions. *Neues Jahrb. Fur Mineral. Abh.* **2015**, *192*, 151–167. [CrossRef]
13. Teiber, H.; Marks, M.A.W.; Wenzel, T.; Siebel, W.; Altherr, R.; Markl, G. The distribution of halogens (F, Cl, Br) in granitoid rocks. *Chem. Geol.* **2014**, *374–375*, 92–109. [CrossRef]
14. Bruand, E.; Fowler, M.; Storey, C.; Darling, J. Apatite trace element and isotope applications to petrogenesis and provenance. *Am. Mineral.* **2017**, *102*, 75–84. [CrossRef]
15. Bromiley, G.D. Do concentrations of Mn, Eu and Ce in apatite reliably record oxygen fugacity in magmas? *Lithos* **2021**, *384–385*, 105900. [CrossRef]
16. Cao, M.-J.; Zhou, Q.-F.; Qin, K.-Z.; Tang, D.-M.; Evans, N.J. The tetrad effect and geochemistry of apatite from the Altay Koktokay No. 3 pegmatite, Xinjiang, China: Implications for pegmatite petrogenesis. *Mineral. Petrol.* **2013**, *107*, 985–1005. [CrossRef]
17. Mao, M.; Rukhlov, A.S.; Rowins, S.M.; Spence, J.; Coogan, L.A. Apatite Trace Element Compositions: A Robust New Tool for Mineral Exploration. *Econ. Geol.* **2016**, *111*, 1187–1222. [CrossRef]
18. Marks, M.A.W.; Scharrer, M.; Ladenburger, S.; Markl, G. Comment on "Apatite: A new redox proxy for silicic magmas?" [Geochimica et Cosmochimica Acta **2014**, *132*, 101–119]. *Geochim. Cosmochim. Acta* **2016**, *183*, 267–270. [CrossRef]
19. Xie, F.; Tang, J.; Chen, Y.; Lang, X. Apatite and zircon geochemistry of Jurassic porphyries in the Xiongcun district, southern Gangdese porphyry copper belt: Implications for petrogenesis and mineralization. *Ore Geol. Rev.* **2018**, *96*, 98–114. [CrossRef]
20. Stokes, T.N.; Bromiley, G.D.; Potts, N.J.; Saunders, K.E.; Miles, A.J. The effect of melt composition and oxygen fugacity on manganese partitioning between apatite and silicate melt. *Chem. Geol.* **2019**, *506*, 162–174. [CrossRef]
21. Sun, S.-J.; Zhang, R.-Q.; Cong, Y.-N.; Zhang, L.-P.; Sun, W.-D.; Li, C.-Y.; Ding, X. Analogous diagenetic conditions of dark enclave and its host granite derived by magma mixing: Evidence for a post-mixing magmatic process. *Lithos* **2020**, *356–357*, 105373. [CrossRef]
22. Belousova, E.A.; Walters, S.; Griffin, W.L.; O'Reilly, S.Y. Trace-element signatures of apatites in granitoids from the Mt Isa Inlier, northwestern Queensland. *Aust. J. Earth Sci.* **2001**, *48*, 603–619. [CrossRef]
23. Decrée, S.; Boulvais, P.; Tack, L.; André, L.; Baele, J.M. Fluorapatite in carbonatite-related phosphate deposits: The case of the Matongo carbonatite (Burundi). *Mineral. Deposita* **2016**, *51*, 453–466. [CrossRef]
24. Duan, D.-F.; Jiang, S.-Y. Using apatite to discriminate synchronous ore-associated and barren granitoid rocks: A case study from the Edong metallogenic district, South China. *Lithos* **2018**, *310–311*, 369–380. [CrossRef]
25. Imai, A. Variation of Cl and SO_3 Contents of Microphenocrystic Apatite in Intermediate to Silicic Igneous Rocks of Cenozoic Japanese Island Arcs: Implications for Porphyry Cu Metallogenesis in the Western Pacific Island Arcs. *Resour. Geol.* **2008**, *54*, 357–372. [CrossRef]
26. Wang, H.; Cai, K.; Sun, M.; Xia, X.-P.; Lai, C.-K.; Li, P.; Wan, B.; Zhang, Z. Apatite as a magma redox indicator and its application in metallogenic research. *Lithos* **2022**, *422–423*, 106749. [CrossRef]
27. Villaseca, C. On the origin of granite types in the Central Iberian Zone: Contribution from integrated U-Pb and Hf isotope studies of zircon. In Proceedings of the VIII Congresso Ibérico de Geoquímica, Castelo Branco, Portugal, 24–28 September 2011; pp. 29–34.
28. Roda-Robles, E.; Villaseca, C.; Pesquera, A.; Gil-Crespo, P.P.; Vieira, R.; Lima, A.; Garate-Olave, I. Petrogenetic relationships between Variscan granitoids and Li-(F-P)-rich aplite-pegmatites in the Central Iberian Zone: Geological and geochemical constraints and implications for other regions from the European Variscides. *Ore Geol. Rev.* **2018**, *95*, 408–430. [CrossRef]

29. Martín-Izard, A.; Reguilón, R.; Palero, F. Las mineralizaciones litiníferas del oeste de Salamanca y Zamora. *Estud. Geológicos* **1992**, *48*, 19–30. [CrossRef]
30. Tornos, F.; Delgado, A.; Casquet, C.; Galindo, C. 300 Million years of episodic hydrothermal activity: Stable isotope evidence from hydrothermal rocks of the Eastern Iberian Central System. *Mineral. Depos.* **2000**, *35*, 551–569. [CrossRef]
31. Neiva, A.M.R. Portuguese granites associated with Sn-W and Au mineralizations. *Bull. Geol. Soc. Finl.* **2002**, *74*, 79–101. [CrossRef]
32. Roda-Robles, E.; Pesquera, A.; Gil-Crespo, P.P.; Vieira, R.; Lima, A.; Garate-Olave, I.; Martins, T.; Torres-Ruiz, J. Geology and mineralogy of Li mineralization in the Central Iberian Zone (Spain and Portugal). *Mineral. Mag.* **2016**, *80*, 103–126. [CrossRef]
33. Llorens, T.; Moro, M.C. Fe-Mn phosphate associations as indicators of the magmatic-hydrothermal and supergene evolution of the Jálama batholith in the Navasfrías Sn-W District, Salamanca, Spain. *Mineral. Mag.* **2012**, *76*, 1–24. [CrossRef]
34. Garate-Olave, I.; Roda-Robles, E.; Gil-Crespo, P.P.; Pesquera, A.; Errandonea-Martin, J. The Tres Arroyos Granitic Aplite-Pegmatite Field (Central Iberian Zone, Spain): Petrogenetic Constraints from Evolution of Nb-Ta-Sn Oxides, Whole-Rock Geochemistry and U-Pb Geochronology. *Minerals* **2020**, *10*, 1008. [CrossRef]
35. Breiter, K.; Ackerman, L.; Svojtka, M.; Müller, A. Behavior of trace elements in quartz from plutons of different geochemical signature: A case study from the Bohemian Massif, Czech Republic. *Lithos* **2013**, *175*, 54–67. [CrossRef]
36. Černý, P.; Burt, D.M. Paragenesis, crystallochemical characteristics, and geochemical evolution of micas in granitic pegmatites. In *Micas*; Bailey, S.W., Ed.; Reviews in Mineralogy; Mineralogical Society of America: Chantilly, Virginia, 1984; Volume 13, pp. 257–298.
37. Garate-Olave, I.; Roda-Robles, E.; Gil-Crespo, P.P.; Pesquera, A. Mica and feldspar as indicators of the evolution of a highly evolved granite-pegmatite system in the Tres Arroyos area (Central Iberian Zone, Spain). *J. Iberian Geol.* **2018**, *44*, 375–403. [CrossRef]
38. Marchal, K.L.; Simmons, W.B.; Falster, A.U.; Webber, K.L.; Roda-Robles, E. Geochemistry, mineralogy, and evolution of Li-Al micas and feldspars from the Mount Mica pegmatite, Maine, USA. *Can. Mineral.* **2014**, *52*, 221–233. [CrossRef]
39. Oyarzabal, J.; Galliski, M.A.; Perino, E. Geochemistry of K-feldspar and Muscovite in Rare-element Pegmatites and Granites from the Totoral Pegmatite Field, San Luis, Argentina. *Resour. Geol.* **2009**, *59*, 315–329. [CrossRef]
40. Roda, E.; Keller, P.; Pesquera, A.; Fontan, F. Micas of the muscovite–lepidolite series from Karibib pegmatites, Namibia. *Mineral. Mag.* **2007**, *71*, 41–62. [CrossRef]
41. Roda-Robles, E.; Vieira, R.; Pesquera, A.; Lima, A. Chemical variations and significance of phosphates from the Fregeneda-Almendra pegmatite field, Central Iberian Zone (Spain and Portugal). *Mineral. Petrol.* **2010**, *100*, 23–34. [CrossRef]
42. Roda-Robles, E.; Pesquera, A.; Gil-Crespo, P.P.; Torres-Ruiz, J. Occurrence, paragenesis and compositional evolution of tourmaline from the Tormes Dome Area, Central Iberian Zone, Spain. *Can. Mineral.* **2011**, *49*, 207–224. [CrossRef]
43. Fransolet, A.M.; Keller, P.; Fontan, F. The phoshate mineral associations of the Tsaobismund pegmatite, Namibia. *Contrib. Mineral. Petrol.* **1986**, *92*, 502–517. [CrossRef]
44. Ginsburg, A.I. Specific geochemical features of the pegmatitic process. In Proceedings of the 21st International Geological Congress Session Norden Report, Copenhagen, Denmark, 1960; Volume 17.
45. Keller, P.; Fontan, F.; Fransolet, A.-M. Intercrystalline cation partitioning between minerals of the triplite-zwieselite-magniotriplite and the triphylite-lithiophilite series in granitic pegmatites. *Contrib. Mineral. Petrol.* **1994**, *118*, 239–248. [CrossRef]
46. Roda-Robles, E.; Pesquera, A.; García de Madinabeitia, S.; Gil-Ibarguchi, J.I.; Nizamoff, J.; Simmons, W.; Falster, A.; Galliski, M.A. On the geochemical character of primary Fe-Mn phosphates belonging to the triphylite-lithiophilite, graftonite-beusite, and triplite-zwieselite series: First results and implications for pegmatite petrogenesis. *Can. Mineral.* **2014**, *52*, 321–335. [CrossRef]
47. Roda-Robles, E.; Pesquera, A.; Gil-Crespo, P.; Torres-Ruiz, J. From granite to highly evolved pegmatite: A case study of the Pinilla de Fermoselle granite–pegmatite system (Zamora, Spain). *Lithos* **2012**, *153*, 192–207. [CrossRef]
48. Roda-Robles, E.; Pesquera, A.; Gil-Crespo, P.P.; Torres-Ruiz, J. The Puentemocha Beryl-Phosphate Granitic Pegmatite, Salamanca, Spain: Internal Structure, Petrography and Mineralogy. *Can. Mineral.* **2012**, *50*, 1573–1587. [CrossRef]
49. Roda-Robles, E.; Pesquera, A.; Simmons, W.; Gil-Crespo, P.P.; Webber, K.; Nizamoff, J.; Falster, A. Paragenetic relationships, geochemistry and petrogenetic significance of primary Fe Mn phosphates from pegmatites: The case study of Cañada (Salamanca, Spain) and Palermo (New Hampshire, USA) pegmatites. *Lithos* **2020**, *374–375*, 105710. [CrossRef]
50. Martínez Catalán, J.R.; Schulmann, K.; Ghienne, J.-F. The Mid-Variscan Allochthon: Keys from correlation, partial retrodeformation and plate-tectonic reconstruction to unlock the geometry of a non-cylindrical belt. *Earth Sci. Rev.* **2021**, *220*, 103700. [CrossRef]
51. Ferreira, N.; Iglesias, M.; Noronha, F.; Pereira, E.; Ribeiro, A.; Ribeiro, M.L. Granitoides da zona Centro-Iberica e seu enquadramento geodinámico. In *Geología de los Granitoides y Rocas Asociadas del Macizo Hespérico. Libro homenaje a L. C. García de Figuerola*; Bea, F., Carnicero, A., Gonzalo, J.C., López Plaza, M., Rodríguez Alonso, M.D., Eds.; Rueda: Madrid, Spain, 1987; pp. 37–53.
52. López-Plaza, M.; Martínez-Catalán, J.R. Síntesis estructural de los granitoides del Macizo Hespérico. In *Geología de los Granitoides y Rocas Asociadas del Macizo Hespérico*; Bea, F., Carnicero, A., Gonzalo, J.C., López-Plaza, M., Rodríguez Alonso, M.D., Eds.; Rueda: Madrid, Spain, 1987; pp. 125–210.
53. Bea, F.; Montero, P.; Zinger, T. The nature, origin, and thermal influence of the granite source layer of Central Iberia. *J. Geol.* **2003**, *111*, 579–595. [CrossRef]
54. Dias, G.; Leterrier, J.; Mendes, A.; Simões, P.P.; Bertrand, J.M. U-Pb zircon and monazite geochronology of post-collisional Hercynian granitoids from the Central Iberian Zone (Northern Portugal). *Lithos* **1998**, *45*, 349–369. [CrossRef]

55. Fernández-Suárez, J.; Dunning, G.R.; Jenner, G.A.; Gutierrez-Alonso, G. Variscan collisional magmatism and deformation in NW Iberia: Constraints from U-Pb geochronology of granitoids. *J. Geol. Soc.* **2000**, *157*, 565–576. [CrossRef]
56. Gutiérrez-Alonso, G.; Fernández-Suárez, J.; Jeffries, T.E.; Johnston, S.T.; Pastor-Galán, D.; Murphy, J.B.; Franco, M.P.; Gonzalo, J.C. Diachronous post-orogenic magmatism within a developing orocline in Iberia, European Variscides. *Tectonics* **2011**, *30*, 17. [CrossRef]
57. Bea, F.; Montero, P.; Molina, J.F. Mafic precursors, peraluminous granitoids, and late lamprophyres in the Avila batholith: A model for the generation of Variscan batholiths in Iberia. *J. Geol.* **1999**, *107*, 399–419. [CrossRef]
58. Dias, G.; Simões, P.P.; Ferreira, N.; Leterrier, J. Mantle and Crustal Sources in the Genesis of Late-Hercynian Granitoids (NW Portugal): Geochemical and Sr-Nd Isotopic Constraints. *Gondwana Res.* **2002**, *5*, 287–305. [CrossRef]
59. Černý, P.; Ercit, T.S. The classification of granitic pegmatites revisited. *Can. Mineral.* **2005**, *43*, 2005–2026. [CrossRef]
60. Antunes, I.M.H.R.; Neiva, A.M.R.; Farinha Ramos, J.M.; Silva, P.B.; Silva, M.M.V.G.; Corfu, F. Petrogenetic links between lepidolite-subtype aplite-pegmatite, aplite veins and associated granites at Segura (central Portugal). *Chem. Erde Geochem.* **2013**, *73*, 323–341. [CrossRef]
61. Gallego Garrido, M. Las Mineralizaciones de Li Asociadas a Magmatismo Acido en Extremadura y su Encuadre en la Zona Centro-Ibérica. Ph.D. Thesis, Universidad Complutense de Madrid, Madrid, Spain, 1992.
62. Garate-Olave, I.; Müller, A.; Roda-Robles, E.; Gil-Crespo, P.P.; Pesquera, A. Extreme fractionation in a granite–pegmatite system documented by quartz chemistry: The case study of Tres Arroyos (Central Iberian Zone, Spain). *Lithos* **2017**, *286–287*, 162–164. [CrossRef]
63. Martins, T.; Roda-Robles, E.; Lima, A.; De Parseval, P. Geochemistry and evolution of micas in the Barroso-Alvão pegmatite field, Northern Portugal. *Can. Mineral.* **2012**, *50*, 1117–1129. [CrossRef]
64. Roda-Robles, E.; Pesquera Pérez, A.; Velasco Roldan, F.; Fontan, F. The granitic pegmatites of the Fregeneda area (Salamanca, Spain): Characteristics and petrogenesis. *Mineral. Mag.* **1999**, *63*, 535–558. [CrossRef]
65. Vieira, R.; Roda-Robles, E.; Pesquera, A.; Lima, A. Chemical variation and significance of micas from the Fregeneda-Almendra pegmatitic field (Central-Iberian Zone, Spain and Portugal). *Am. Mineral.* **2011**, *96*, 637–645. [CrossRef]
66. Lima, A. Estrutura, Mineralogia e Génese dos Filões Aplitopegmatíticos com Espodumena da Região do Barroso-Alvão (Norte de Portugal). Ph.D. Thesis, Univ. Porto, Porto, Portugal, Institut National Polytechnique de Lorraine, Nancy, France, 2000; 270p.
67. Neiva, A.M.R.; Ramos, J.M.F. Geochemistry of granitic aplite-pegmatite sills and petrogenetic links with granites, Guarda-Belmonte area, central Portugal. *Eur. J. Mineral.* **2010**, *22*, 837–854. [CrossRef]
68. Pesquera, A.; Roda-Robles, E.; Gil-Crespo, P.P.; Valls, D.; Ruiz, J.T. The metasomatic enrichment of Li in psammopelitic units at San José-Valdeflórez, Central Iberian Zone, Spain: A new type of lithium deposit. *Sci. Rep.* **2020**, *10*, 10828. [CrossRef]
69. Ferrerira, N.; Vieira, G. *Guia Geológico e Geomorfológico do Parque Natural da Serra da Estrela—Locais de Interesse Geológico e Geomorfológico*; Instituto da Conservação da Naturaleza—Instituto Geológico e Mineiro: Alfragide, Portugal, 1999; 111p.
70. Garate-Olave, I.; Roda Robles, E.; Gil-crespo, P.P.; Müller, A.; Pesquera, A. El Sistema Granito-Pegmatita de Tres Arroyos (Alburquerque, Badajoz): Petrografía, Mineralogía y Modelo Petrogenético. *Macla* **2016**, *21*, 41–43.
71. Capdevila, R.; Corretgé, L.G.; Floor, P. Les granitoides Varisques de la Meseta Ibérique. *Bull. Soc. Géol. Fr.* **1973**, *S7-XV*, 209–228. [CrossRef]
72. Gomes, M.E.P.; Teixeira, R.J.S.; Neiva, A.M.R.; Corfu, F. Geochemistry and geochronology of granitoids from Bemposta-Picote region, Northeastern Portugal. *Comun. Geol.* **2014**, *101*, 115–118.
73. López-Moro, F.J.; López-Plaza, M.; Romer, R.L. Generation and emplacement of shear-related highly mobile crustal melts: The synkinematic leucogranites from the Variscan Tormes Dome, Western Spain. *Int. J. Earth Sci.* **2012**, *101*, 1273–1298. [CrossRef]
74. Teixeira, R.J.S.; Neiva, A.M.R.; Gomes, M.E.P.; Corfu, F.; Cuesta, A.; Croudace, I.W. The role of fractional crystallization in the genesis of early syn-D3, tin-mineralized Variscan two-mica granites from the Carrazeda de Ansiães area, northern Portugal. *Lithos* **2012**, *153*, 177–191. [CrossRef]
75. Cuesta, A.; Gallastegui, G. Galicia Occidental. In *Geología de España*; Vera, J.A., Ed.; SGE-IGME: Madrid, Spain, 2004; pp. 96–100.
76. Ortega, L. Estudio petrogenético del granito sincinemático de dos micas de A Espenuca (A Coruña). *Lab. Xeolóxico Laxe Ser. Nova Terra* **1998**, *14*, 377.
77. Almeida, A.; Leterrier, J.; Noronha, F.; Bertrand, J.M. U-Pb zircon and monazite geochronology of the hercynian two-mica granite composite pluton of Cabeceiras de Basto (Northern Portugal). *Comptes Rendus L'académie Sci. Ser. IIA—Earth Planet. Sci.* **1998**, *326*, 779–785. [CrossRef]
78. Antunes, I.M.H.R.; Neiva, A.M.R.; Silva, M.M.V.G.; Corfu, F. Geochemistry of S-type granitic rocks from the reversely zoned Castelo Branco pluton (central Portugal). *Lithos* **2008**, *103*, 445–465. [CrossRef]
79. Chicharro, E.; Villaseca, C.; Valverde-Vaquero, P.; Belousova, E.; López-Garcia, J.A. Zircon U-Pb and Hf isotopic constraints on the genesis of a post-kinematic S-type Variscan tin granite: The Logrosan cupola (Central Iberian Zone). *J. Iberian Geol.* **2014**, *40*, 451–470. [CrossRef]
80. Merino Martínez, E.; Villaseca, C.; Orejana, D.; Pérez-Soba, C.; Belousova, E.; Andersen, T. Tracing magma sources of three different S-type peraluminous granitoid series by in situ U–Pb geochronology and Hf isotope zircon composition: The Variscan Montes de Toledo batholith (central Spain). *Lithos* **2014**, *200–201*, 273–298. [CrossRef]
81. Ramírez, J.A.; Menéndez, L. A geochemical study of two peraluminous granites from south-central Iberia: The Nisa-Albuquerque and Jalama batholiths. *Mineral. Mag.* **1999**, *63*, 85–104. [CrossRef]

82. Errandonea-Martin, J.; Sarrionandia, F.; Janousek, V.; Carracedo-Sánchez, M.; Gil-Ibarguchi, J.I. Origin of cordierite-bearing monzogranites from the southern Central Iberian Zone—Inferences from the zoned Sierra Bermeja Pluton (Extremadura, Spain). *Lithos* **2019**, *342–343*, 440–462. [CrossRef]
83. Pesquera, A.; Gil-Crespo, P.P.; Torres-Ruiz, J.; Roda-Robles, E. Insights into petrogenesis of the Jálama pluton (Central Iberian Zone, western Spain). *Int. Geol. Rev.* **2018**, *60*, 157–187. [CrossRef]
84. González-Menéndez, L.; Azor, A.; Rubio-Ordóñez, Á.; Sánchez-Almazo, I. The metamorphic aureole of the Nisa-Alburquerque batholith (SW Iberia): Implications for deep structure and emplacement mode. *Int. J. Earth Sci.* **2011**, *100*, 1533–1550. [CrossRef]
85. Merino, E.; Villaseca, C.; Orejana, D.; Jeffries, T. Gahnite, chrysoberyl and beryl co-occurrence as accessory minerals in a highly evolved peraluminous pluton: The Belvís de Monroy leucogranite (Cáceres, Spain). *Lithos* **2013**, *179*, 137–156. [CrossRef]
86. Merino Martínez, E. Geochemistry, U–Pb Geochronology and Hf-Isotope Zircon Composition of Variscan Granitoids from the Montes de Toledo Batholith. Ph.D. Thesis, Universidad Complutense de Madrid, Madrid, Spain, 2014.
87. Vindel, E.; Chicharro, E.; Villaseca, C.; López-García, J.Á.; Sánchez, V. Hydrothermal phosphate vein-type ores from the southern Central Iberian Zone, Spain: Evidence for their relationship to granites and Neoproterozoic metasedimentary rocks. *Ore Geol. Rev.* **2014**, *62*, 143–155. [CrossRef]
88. Neiva, A.M.R.; Silva, P.B.; Ramos, J.M.F. Geochemistry of granitic aplite-pegmatite veins and sills and their minerals from Cabeço dos Poupos, Sabugal, Central Portugal. *Asoc. Geológica Argent. Ser. D Publicación Espec.* **2011**, *143*, 141–143. [CrossRef]
89. Martínez-Catalán, J.R.; Martínez Poyatos, D.; Bea, F. Zona Centroibérica: Introducción. In *Geología de España*; Vera, J.A., Ed.; SGE-IGME: Madrid, Spain, 2004; pp. 68–69.
90. Garate-Olave, I. Petrography, Mineralogy and Origin of the Rare Elements Granitic Aplopegmatites from Tres Arroyos (Badajoz, Spain). Ph.D. Thesis, Universidad del País Vasco (UPV/EHU), Leioa, Spain, 2018.
91. Garate-Olave, I.; Roda-Robles, E.; Gil-Crespo, P.P.; Pesquera, A. The phosphate mineral associations from the Tres Arroyos aplite-pegmatites (Badajoz, Spain): Petrography, mineral chemistry and petrogenetic implications. *Can. Mineral.* **2020**, *58*, 747–765. [CrossRef]
92. Martins, T. Multidisciplinary Study of Pegmatites and Associated Li and SN-Nb-Ta Mineralisation from the Barroso-Alvão Region. Ph.D. Thesis, Universidade do Porto, Porto, Portugal, 2009.
93. Llorens, T. Las Mineralizaciones Magmático-Hidrotermales de Sn-W(Nb-Ta) del Distrito de Navasfrías (SO de Salamanca). Ph.D. Thesis, Universidad de Salamanca, Salamanca, Spain, 2011.
94. Roda, E.; Pesquera, A.; Fontan, F.; Keller, P. Phosphate mineral associations in the Cañada pegmatite (Salamanca, Spain): Paragenetic relationships, chemical compositions, and implications for pegmatite evolution. *Am. Mineral.* **2004**, *89*, 110–125. [CrossRef]
95. London, D.; Wolf, M.B.; Morgan, G.B.; Gallego-Garrido, M. Experimental Silicate–Phosphate Equilibria in Peraluminous Granitic Magmas, with a Case Study of the Alburquerque Batholith at Tres Arroyos, Badajoz, Spain. *J. Petrol.* **1999**, *40*, 215–240. [CrossRef]
96. Roda-Robles, E.; Pesquera, A.; Gil-Crespo, P.P.; Garate-Olave, I.; Torres-Ruiz, J. The Li-Rich Aplopegmatite from Castillejo de Dos Casas (Salamanca, Spain): Example of a Highly Fractionated Granite-Pegmatite System. In Proceedings of the 13th Biennial SGA Meeting, Nancy, France, 24–27 August 2015; Volume 2, pp. 835–838.
97. Fuertes-Fuente, M. Las Pegmatitas del Area de Lalín-Forcarey (Galicia) y las Mineralizaciones de Elementos Escasos Asociadas. Ph.D. Thesis, Universidad de Oviedo, Oviedo, Spain, 1996.
98. Carvalho, J.M.F.; Farinha, J.A.L.B. Lithium potentialities in Northern Portugal. In Proceedings of the 17th Industrial Minerals International Congress, Barcelona, Spain, 28–31 March 2004; pp. 1–10.
99. Cardoso-Fernandes, J.; Santos, D.; Lima, A.; Teodoro, A.C.; Perrotta, E.; Roda-Robles, E. Validation of Remote Sensing Techniques in Greenfield Exploration Areas for Lithium (LI) in Central Portugal: A Study Case. In Proceedings of the 2021 IEEE International Geoscience and Remote Sensing Symposium IGARSS, Brussels, Belgium, 11–16 July 2021; pp. 6622–6625.
100. Garate-Olave, I.; Roda-Robles, E.; Gil-Crespo, P.P.; Pesquera-Pérez, A.; Vieira, R.; Lima, A. Estudio textural y Mineralógico del Dique de Cuarzo con Fosfatos de Folgosinho (Guarda, Portugal). *Macla* **2012**, *16*, 220–221.
101. Pouchou, J.L.; Pichoir, F. "PAP" φ(ρZ) procedure for improved quantitative microanalysis. In *Microbean Analysis*; Armstrong, J.T., Ed.; San Francisco Press: San Francisco, CA, USA, 1985; pp. 104–106.
102. Pérez-Soba, C.; Villaseca, C.; Fernández, A. Magmatic graphite inclusions in Mn-Fe-rich fluorapatite of perphosphorus granites (the Belvís pluton, Variscan Iberian Belt). *Am. Mineral.* **2017**, *102*, 728–742. [CrossRef]
103. Errandonea-Martin, J. Petrology of Cordierite-Bearing Monzogranites and Related Mesocratic Rocks from the Sierra Bermeja Pluton (Southern Iberian Massif). Ph.D. Thesis, Universidad del País Vasco (UPV/EHU), Leioa, Spain, 2019.
104. Paton, C.; Hellstrom, J.; Paul, B.; Woodhead, J.; Hergt, J. Iolite: Freeware for the visualisation and processing of mass spectrometric data. *J. Anal. At. Spectrom.* **2011**, *26*, 2508–2518. [CrossRef]
105. Paul, B.; Paton, C.; Norris, A.; Woodhead, J.; Hellstrom, J.; Hergt, J.; Greig, A. CellSpace: A module for creating spatially registered laser ablation images within the Iolite freeware environment. *J. Anal. At. Spectrom.* **2012**, *27*, 700–706. [CrossRef]
106. McDonough, W.; Sun, S.S. The composition of the Earth. *Chem. Geol.* **1995**, *67*, 1050–1056. [CrossRef]
107. Irber, W. The lanthanide tetrad effect and its correlation with K/Rb, Eu/Eu*, Sr/Eu, Y/Ho, and Zr/Hf of evolving peraluminous granite suites. *Geochim. Cosmochim. Acta* **1999**, *63*, 489–508. [CrossRef]
108. Pieczka, A. Beusite and an unusual Mn-rich apatite from the Szklary granitic pegmatite, Lower Silesia, Southwestern Poland. *Can. Mineral.* **2007**, *45*, 901–914. [CrossRef]

109. Miles, A.J.; Graham, C.M.; Hawkesworth, C.J.; Gillespie, M.R.; Hinton, R.W.; Bromiley, G.D. Apatite: A new redox proxy for silicic magmas? *Geochim. Cosmochim. Acta* **2014**, *132*, 101–119. [CrossRef]
110. O'Sullivan, G.; Chew, D.; Kenny, G.; Henrichs, I.; Mulligan, D. The trace element composition of apatite and its application to detrital provenance studies. *Earth Sci. Rev.* **2020**, *201*, 103044. [CrossRef]
111. Stokes, T.N. *The Crystal Chemistry of Accessory Minerals as a Probe of Magmatic Oxygen Fugacity: An Experimental Study*; University of Edinburgh: Edinburgh, Scotland, 2018.
112. Villaseca, C.; Ruiz-Martinez, C.C.; Péraz-Soba, C. Magnetic susceptibility of Variscan granite-types of the Spanish Central System and the redox state of magma. *Geol. Acta* **2017**, *15*, 379–394. [CrossRef]
113. Pichavant, M.; Villaros, A.; Deveaud, S.; Scaillet, B.; Lahlafi, M. The Influence of Redox State on Mica Crystallization in Leucogranitic and Pegmatitic Liquids. *Can. Mineral.* **2016**, *54*, 559–581. [CrossRef]
114. Puziewicz, J.; Johannes, W. Experimental study of a biotite bearing granitic system under water saturated and water undersaturated conditions. *Contrib. Mineral. Petrol.* **1990**, *104*, 397–406. [CrossRef]
115. Wones, D.R.; Eugster, H.P. Stability of biotite: Experiment, Theory, and Application. *Am. Mineral.* **1965**, *50*, 1228–1272.
116. Harrison, T.M.; Watson, E.B. The behavior of apatite during crustal anatexis: Equilibrium and kinetic considerations. *Geochim. Cosmochim. Acta* **1984**, *48*, 1467–1477. [CrossRef]
117. Mysen, B.; Richet, P. *Silicate Glasses and Melts*; Elsevier: Amsterdam, The Netherlands, 2005.
118. Keppler, H. Partitioning of phosphorus between melt and fluid in the system haplogranite-H_2O-P_2O_5. *Chem. Geol.* **1994**, *117*, 345–353. [CrossRef]
119. London, D. Internal differentiation of rare-element pegmatites: Effects of boron, phosphorus, and fluorine. *Geochim. Cosmochim. Acta* **1987**, *51*, 403–420. [CrossRef]
120. Roda, E.; Pesquera, A.; Gil-Crespo, P.P.; Torres-Ruiz, J.; Fontan, F. Origin and internal evolution of the Li-F-Be-B-P-bearing Pinilla de Fermoselle pegmatite (Central Iberian Zone, Zamora, Spain). *Am. Mineral.* **2005**, *90*, 1887–1899. [CrossRef]
121. Roda-Robles, E.; Fontan, F.; Pesquera, A.; Keller, P. The Fe-Mn phosphate associations from the Pinilla de Fermoselle pegmatite, Zamora, Spain: Occurrence of kryzhanovskite and natrodufrenite. *Eur. J. Mineral.* **1998**, *10*, 155–167. [CrossRef]
122. Rutherford, M.J.; Hess, P.C.; Daniel, G.H. Experimental liquid line of descent and liquid immiscibility for basalt 70017. In Proceedings of the Lunar and Planetary Science Conference Proceedings, Houston, TX, USA, 18–22 March 1974; Volume 1, pp. 569–583.
123. James, P.F.; Mcmillan, P.W. Quantitative measurements of phase separation in glasses using transmission electron microscopy. Part 2. A study of lithia-silica glasses and the influence of phosphorus pentoxide. *Phys. Chem. Glasses* **1970**, *11*, 64–70.
124. Prowatke, S.; Klemme, S. Trace element partitioning between apatite and silicate melts. *Geochim. Cosmochim. Acta* **2006**, *70*, 4513–4527. [CrossRef]
125. Hughes, J.M.; Rakovan, J. Structurally Robust, Chemically Diverse: Apatite and Apatite Supergroup Minerals. *Elements* **2015**, *11*, 165–170. [CrossRef]
126. Schettler, G.; Gottschalk, M.; Harlov, D.E. A new semi-micro wet chemical method for apatite analysis and its application to the crystal chemistry of fluorapatite-chlorapatite solid solutions. *Am. Mineral.* **2011**, *96*, 138–152. [CrossRef]
127. Zhu, C.; Sverjensky, D.A. Partitioning of F-Cl-OH between minerals and hydrothermal fluids. *Geochim. Cosmochim. Acta* **1991**, *55*, 1837–1858. [CrossRef]
128. Ding, T.; Ma, D.; Lu, J.; Zhang, R. Apatite in granitoids related to polymetallic mineral deposits in southeastern Hunan Province, Shi–Hang zone, China: Implications for petrogenesis and metallogenesis. *Ore Geol. Rev.* **2015**, *69*, 104–117. [CrossRef]
129. Webster, J.D.; Piccoli, P.M. Magmatic Apatite: A Powerful, Yet Deceptive, Mineral. *Elements* **2015**, *11*, 177–182. [CrossRef]
130. Burnham, A.D.; Berry, A.J. The effect of oxygen fugacity, melt composition, temperature and pressure on the oxidation state of cerium in silicate melts. *Chem. Geol.* **2014**, *366*, 52–60. [CrossRef]
131. Burnham, A.D.; Berry, A.J.; Halse, H.R.; Schofield, P.F.; Cibin, G.; Mosselmans, J.F.W. The oxidation state of europium in silicate melts as a function of oxygen fugacity, composition and temperature. *Chem. Geol.* **2015**, *411*, 248–259. [CrossRef]
132. Sha, L.K.; Chappell, B.W. Apatite chemical composition, determined by electron microprobe and laser-ablation inductively coupled plasma mass spectrometry, as a probe into granite petrogenesis. *Geochim. Cosmochim. Acta* **1999**, *63*, 3861–3881. [CrossRef]
133. Duan, X.-X.; Chen, B.; Sun, K.-K.; Wang, Z.-Q.; Yan, X.; Zhang, Z. Accessory mineral chemistry as a monitor of petrogenetic and metallogenetic processes: A comparative study of zircon and apatite from Wushan Cu- and Zhuxiling W(Mo)-mineralization-related granitoids. *Ore Geol. Rev.* **2019**, *111*, 102940. [CrossRef]
134. Pan, L.-C.; Hu, R.-Z.; Wang, X.-S.; Bi, X.-W.; Zhu, J.-J.; Li, C. Apatite trace element and halogen compositions as petrogenetic-metallogenic indicators: Examples from four granite plutons in the Sanjiang region, SW China. *Lithos* **2016**, *254–255*, 118–130. [CrossRef]
135. Kontak, D.J.; Martin, R.F. Alkali feldspar in the peraluminous South Mountain Batholith, Nova Scotia: Trace-element data. *Can. Mineral.* **1997**, *35*, 959–977.
136. Abdullin, F.; Solé, J.; Solari, L.; Shchepetilnikova, V.; Meneses-Rocha, J.J.; Pavlinova, N.; Rodríguez-Trejo, A. Single-grain apatite geochemistry of Permian–Triassic granitoids and Mesozoic and Eocene sandstones from Chiapas, southeast Mexico: Implications for sediment provenance. *Int. Geol. Rev.* **2016**, *58*, 1132–1157. [CrossRef]
137. Ballard, J.R.; Palin, M.J.; Campbell, I.H. Relative oxidation states of magmas inferred from Ce(IV)/Ce(III) in zircon: Application to porphyry copper deposits of northern Chile. *Contrib. Mineral. Petrol.* **2002**, *144*, 347–364. [CrossRef]

138. Drake, M.J.; Weill, D.F. Partition of Sr, Ba, Ca, Y, Eu^{2+}, Eu^{3+}, and other REE between plagioclase feldspar and magmatic liquid: An experimental study. *Geochim. Cosmochim. Acta* **1975**, *39*, 689–712. [CrossRef]
139. Abramov, S.S. Modeling of REE fractionation in the acid melt-fluoride-chloride fluid system. *Dokl. Earth Sci.* **2001**, *377*, 198–200.
140. Muecke, G.K.; Clarke, D.B. Geochemical evolution of the South Mountain Batholith, Nova Scotia; rare-earth-element evidence. *Can. Mineral.* **1981**, *19*, 133–145.
141. Candela, P.A. Theoretical constraints on the chemistry of the magmatic aqueous phase. In *Ore-Bearing Granite Systems, Petrogenesis and Mineralizaing Processes*; Stein, H.J., Hannah, J.L., Eds.; Geological Society of America: Boulder, CO, USA, 1990; Volume 246, pp. 11–19.
142. Yu, M.; Xia, Q.-X.; Zheng, Y.-F.; Zhao, Z.-F.; Chen, Y.-X.; Chen, R.-X.; Luo, X.; Li, W.-C.; Xu, H. The composition of garnet in granite and pegmatite from the Gangdese orogen in southeastern Tibet: Constraints on pegmatite petrogenesis. *Am. Mineral.* **2021**, *106*, 265–281. [CrossRef]
143. Watson, E.B.; Green, T.H. Apatite/liquid partition coefficients for the rare earth elements and strontium. *Earth Planet. Sci. Lett.* **1981**, *56*, 405–421. [CrossRef]
144. RØnsbo, J.G. Coupled substitutions involving REEs and Na and Si in apatites in alkaline rocks from the Ilimaussaq Intrusion, South Greenland, and the petrological implications. *Am. Mineral.* **1989**, *74*, 896–901.
145. Bau, M. Controls on the fractionation of isovalent trace elements in magmatic and aqueous systems: Evidence from Y/Ho, Zr/Hf, and lanthanide tetrad effect. *Contrib. Mineral. Petrol.* **1996**, *123*, 323–333. [CrossRef]
146. Dolejs, D.; Stemprok, M. Magmatic and hydrothermal evolution of Li-F granites: Cinovec and Krasno intrusions, Krusne hory batholith, Czech Republic. *Bull. Geosci.* **2001**, *76*, 77–99.
147. Kawabe, I. Tetrad effects and fine structures of REE abundance patterns of granitic and rhyolitic rocks: ICP-AES determinations of REE and Y in eight GSJ reference rocks. *Geochem. J.* **1995**, *29*, 213–230. [CrossRef]
148. Monecke, T.; Kempe, U.; Monecke, J.; Sala, M.; Wolf, D. Tetrad effect in rare earth element distribution patterns: A method of quantification with application to rock and mineral samples from granite-related rare metal deposits. *Geochim. Cosmochim. Acta* **2002**, *66*, 1185–1196. [CrossRef]
149. Zhao, Z.; Xiong, L.; Hen, X.D.; Wang, Y.X.; Wang, Q.; Bao, Z.; Jahn, B. Controls on the REE tetrad effect in granites: Evidence from the Qianlishan and Baerzhe granites, China. *Geochem. J.* **2002**, *36*, 527–543.
150. Cardoso-Fernandes, J.; Lima, A.; Roda-Robles, E.; Ribeiro, M.D.A.; Teodoro, A.C. Vectoring Lithium (Li) Mineralizations: A First Approach to Pegmatite Geochemical Halo Definition in the Fregeneda-Almendra Area. In Proceedings of the Goldschmidt, Lyon, France, 4–9 July 2021.
151. Anders, E.; Grevesse, N. Abundances of the elements: Meteoritic and solar. *Geochim. Cosmochim. Acta* **1989**, *53*, 197–214. [CrossRef]
152. Peretyazhko, I.S.; Savina, E.A. Tetrad effects in the rare earth element patterns of granitoid rocks as an indicator of fluoride-silicate liquid immiscibility in magmatic systems. *Petrology* **2010**, *18*, 514–543. [CrossRef]
153. Bea, F. Residence of REE, Y, Th and U in granites and crustal protoliths; Implications for the chemistry of crustal melts. *J. Petrol.* **1996**, *37*, 521–552. [CrossRef]
154. Cheng, Y.; Xu, Z.; Di, H.; Zhang, Z.; Mao, C.; Tan, H.; Huang, J.; Zhou, F.; Zhang, L.; Chen, J.; et al. Apatite U-Pb Dating and Composition Constraints for Magmatic–Hydrothermal Evolution in the Giant Renli Nb-Ta Deposit, South China. *Minerals* **2022**, *12*, 344. [CrossRef]
155. Pan, Y.; Breaks, F.W. Rare-earth elements in fluorapatite, separation lake area, Ontario: Evidence for S-type granite—Rare-element pegmatite linkage. *Can. Mineral.* **1997**, *35*, 659–671.
156. Boswell, J.T. Porphyry system fertility discrimination and mineralization vectoring using igneous apatite substitutions to derive pre-exsolution melt mineralization component concentrations. Master's Thesis, The University of Utah, Salt Lake City, UT, USA, 2014.
157. Imai, A. Metallogenesis of Porphyry Cu Deposits of the Western Luzon Arc, Philippines: K-Ar ages, SO_3 Contents of Microphenocrystic Apatite and Significance of Intrusive Rocks. *Resour. Geol.* **2002**, *52*, 147–161. [CrossRef]